Scope of self-interacting thermal WIMPs in a minimal $U(1)_D$ extension and its future prospects

Rahool Kumar Barman,[a] **Biplob Bhattacherjee,**[a] **Arindam Chatterjee,**[b] **Arghya Choudhury**[c] **and Aritra Gupta**[d]

[a] *Centre for High Energy Physics, Indian Institute of Science, Bangalore 560012, India*

[b] *Indian Statistical Institute, 203 B.T. Road, Kolkata, India*

[c] *Department of Physics, Indian Institute of Technology Patna, Bihta, 801103, India*

[d] *Tata Institute of Fundamental Research, Homi Bhabha Road, Mumbai, 400005, India*

E-mail: rahoolbarman@iisc.ac.in, biplob@iisc.ac.in, arindam.chatterjee@gmail.com, arghya@iitp.ac.in, aritragupta@theory.tifr.res.in

ABSTRACT: In this work we have considered a minimal extension of Standard Model by a local U(1) gauge group in order to accommodate a stable (fermionic) Dark Matter (DM) candidate. We have focussed on parameter regions where DM possesses adequate self-interaction, owing to the presence of a light scalar mediator (the dark Higgs), alleviating some of the tensions in the small-scale structures. We have studied the scenario in the light of a variety of data, mostly from dark matter direct searches, collider searches and flavor physics experiments, with an attempt to constrain the interactions of the standard model (SM) particles with the ones in the Dark Sector (DS). Assuming a small gauge kinetic mixing parameter, we find that for rather heavy DM the most stringent bound on the mixing angle of the Dark Higgs with the SM Higgs boson comes from dark matter direct detection experiments, while for lighter DM, LHC constraints become more relevant. Note that, due to the presence of very light mediators, the effective operator approach to the direct detection is inapplicable here and these constraints have been re-evaluated for our scenario. In addition, we find that the smallness of the relevant portal couplings, as dictated by data, critically suppress the viability of DM production by the standard "freeze-out" mechanism in such simplified scenarios. In particular, the viable DM masses are $\lesssim \mathcal{O}(2)\,\mathrm{GeV}$ i.e. in the regions where direct detection limits tend to become weak. For heavier DM with large self-interactions, we hence conclude that non-thermal production mechanisms are favored. Lastly, future collider reach of such a simplified scenario has also been studied in detail.

Contents

1 Introduction

The evidence for existence of non-relativistic non-luminous Dark Matter (DM) has been overwhelming. Several astrophysical and cosmological observations have indicated the presence of DM [1]. Within the paradigm of the standard model of cosmology (ΛCDM) recent measurements of the Cosmic Microwave Background Radiation (CMBR) estimated that about 26% of the energy budget of our Universe consists of DM [2, 3].[1] CMBR, together with Big Bang Nucleosynthesis (BBN) requires DM to be non-baryonic. Astro-physical objects, especially primordial black holes (PBHs) have been considered as DM candidates. While such PBHs, for certain windows of mass[2] can account for the entire energy budget of DM, it has been shown that adequate production of PBHs after (single-field slow-roll) inflation can be difficult [7, 8]. However, the standard model (SM) of particle physics, does not incorporate any suitable DM candidate. Various extensions of the SM has been considered in the literature [9, 10]. A generic aspect in DM models concerns about the stability of DM. Constraints from structure formation, indirect searches [11–13] and CMB [14] require DM to be very long-lived (life-time $\tau \gtrsim 10^{26}$ s depending on the decay modes). The simplest models introduce a global symmetry to prevent the decay of DM. However, it has been argued that such global symmetries may be broken due to gravitational effects [15–17]. This, in turn, can induce Planck-scale suppressed effective terms contributing to the decay of the DM [18]. In this article, therefore, we extend the SM with a simple continuous local symmetry U(1). We further assume that the DM is charged under this symmetry, and therefore, is stable. Earlier works that also explored simplest extensions of Standard Model with similar phenomenological signatures can be found in [19–26]

Recent results from the Large Hadron Collider (LHC), so far, present no convincing evidence for new physics, see e.g. [27–29] for implications on DM models. Further, no evidence for particle DM has emerged from direct [30–32] (and indirect [33, 34]) searches of DM. The Standard Model (SM) of particle physics remains a good low energy effective description. Stringent constraints on most well-motivated new physics scenarios present two distinct possibilities: any new physics may be beyond the energy reach of the LHC, and perhaps can only be probed indirectly through their contribution to the higher dimensional effective operators; or new physics, if exists at (or below) the electroweak scale, may be very weakly coupled to the SM. In the subsequent discussion, we will assume the latter and consider the Dark Sector (DS) particles to be accessible at LHC.

There is an additional motivation for this consideration. Note that in spite of the enormous success of ΛCDM in the cosmological scales, there have been concerns, in particular when it comes to the small scale structures (see e.g. [35–37] for recent reviews). The most notable ones include *Core-vs-cusp* [38, 39] and *Too-big-to-fail* [40–43].[3] It has been argued that self-interacting DM can also simultaneously resolve these issues [48, 49], see

---

[1]Very similar estimates have been obtained for simple extensions of ΛCDM and for ωCDM models.

[2]According to [4], the allowed regions span the following range $(10^{16} - 10^{17}, 10^{20} - 10^{24}, 10^{33} - 10^{36})$ gm. While the mass range $10^{16} - 10^{17}$ gm is claimed to be disfavored by EDGES [1, 5], observations by Subaru/HSC further disfavors the mass range $10^{22} - 10^{27}$ gm [6].

[3]*Missing satellite* problem [44, 45] has also been extensively discussed. However, the discovery of faint dwarfs has lead to dissolution of this issue [46, 47].

also [50, 51] for a review. Although this requires a very large self-interaction cross-section, it remains consistent with the present constraints on DM self-interaction [52–55].[4,5,6] Further, it has been argued that a velocity dependent self-interaction cross-section is favoured [62]. In the presence of light mediators, it is possible to generate large (velocity dependent) self-interaction among DM particles, thanks to the Sommerfeld enhanced self scattering cross-section [51, 63–66]. In the present work, we will ensure that the U(1) extended DS consists of at least one light mediator which facilitate adequate self-interaction among the DM particles. Imposing these criteria, we will investigate the implications on this simple DS. Further, combining constraints from collider searches, flavor physics, beam dump experiments and direct detection of DM, we will try to put restrictions on its interaction with the SM sector.

This article is organised as follows: in section 2 we describe the minimal U(1)$_D$ model and its particle content in detail. In section 3 the parameter space relevant for the study of large self-interaction of dark matter is motivated quantitatively. Next, concentrating on the light H_1 region as motivated from self-interactions, impact of several experiments (like beam dump, flavor physics and collider) on our parameter space of interest is described studied in section 4 and section 5. Section 6 deals with bounds from dark matter phenomenology and discusses its implications. In section 7 we have presented a detailed study about the future prospects of our scenario from a collider perspective. Finally we summarize and conclude in section 8.

2   Description of the model

As described in the introduction, we consider a simple extension of SM where the stability of DM has been attributed to a local symmetry. However, any unbroken local symmetry would imply the existence of a massless gauge boson. Cosmological observations together with the success of BBN constrain the presence of such a boson through the tight limits of extra relativistic *dof*. This demands the U(1)$_D$ to be broken, and we employ Higgs mechanism to achieve this.[7]

We have assumed minimal particle content for a Dark Sector with a local U(1)$_D$ gauge symmetry. Two Weyl fermions needed to be introduced so that the gauge anomaly associated with U(1)$_D$ group cancels, and the theory remains anomaly free. We will further elaborate on the motivation behind this particular choice. The Dark Sector is assumed to have the following particle content: In table 1, ξ_1 and ξ_2 represents left-chiral Weyl

---

[4]See also [50] and references there for a compilation of constraints from bullet-cluster [56–58], ellipticity of the halos and substructure mergers.

[5]An observed separation between the stars of a galaxy and the DM halo, while the galaxy falls into the core of a galaxy cluster Abel 3827, has been recently observed [59]. When interpreted as due to DM self-interaction, this leads to $\frac{\sigma}{m} \simeq 1.5(3)$ cm^{2}gm^{-1} for contact (long-range) interactions [60]. However, the data has been argued to be also consistent with standard collisionless DM [61].

[6]While baryonic feedback can possibly address some of these issues, it has been argued to face difficulties in the context of field galaxies. For a review see [50].

[7]An Abelian gauge boson can also get massive via Stuckelberg mechanism [67–70], which essentially assumes the neutral scalar component to be very heavy and therefore decoupled from the spectrum. However, we will not consider that possibility here.

Particles (spin)	ξ_1 ($\frac{1}{2}$)	ξ_2 ($\frac{1}{2}$)	φ (0)	Z_D (1)
U(1)$_D$ charge (q_D)	1	-1	2	0

Table 1. Particle content (in the gauge eigenbasis) of the Dark Sector (DS) and their charges (q_D) under U(1)$_D$ gauge group.

spinors, while Z_D and φ represents a vector boson and a complex scalar field respectively. We consider the following lagrangian, which is invariant under $\mathcal{G}_{\text{SM}} \times \text{U}(1)_D$ (where, $\mathcal{G}_{\text{SM}}$ denotes the SM gauge group).

$$\mathcal{L} = \mathcal{L}_{\text{SM}} + \mathcal{L}_{\text{DS}} + \mathcal{L}_{\text{portal}}; \tag{2.1}$$

where "DS" and "portal" denote Dark Sector and mediator respectively. The two component Weyl spinors ξ_1 and ξ_2 can be expressed as a four component fermion $\chi = (\xi_1, \tilde{\xi}_2)^T$, where $\tilde{\xi}_j = -i\sigma_2 \xi_j^*$. With this notation, we have,

$$\mathcal{L}_{\text{DS}} = i\overline{\chi}\gamma^\mu D_\mu \chi + D_\mu \varphi^* D^\mu \varphi - V(\varphi) - M\overline{\chi}\chi - \left(\frac{f}{\sqrt{2}} \varphi \overline{\chi} \chi^c + h.c. \right). \tag{2.2}$$

where γ_μ in the Weyl representation has been assumed. Further, in the lagrangian above $D^\mu = \partial^\mu - ig_D q_D Z_D^\mu$ and $\chi^c = i\gamma_2 \gamma_0 \overline{\chi}^T = (\xi_2, \tilde{\xi}_1)^T$. Note that a U(1)$_D$ charge of $1(-1)$ for χ ($\tilde{\chi}$) together with a charge of ∓ 2 for φ ensures the invariance of the Yukawa term under the gauge group U(1)$_D$.

The Dark Sector interacts with the SM sector via the following gauge invariant terms.

$$\mathcal{L}_{\text{portal}} = -\frac{\epsilon_g}{4} F^{\mu\nu} F_{D\mu\nu} - \frac{\lambda_{\text{mix}}}{4} (\varphi^* \varphi)(H^\dagger H), \tag{2.3}$$

Although none of the particles in the low energy spectrum are charged under both U(1)$_Y$ and U(1)$_D$ gauge symmetry, we still keep the gauge invariant phenomenologically viable kinetic mixing term [71] in the lagrangian, which can possibly be generated due to high-scale physics. We parametrize the mixing term with parameter ϵ_g. The scalar field φ can couple with the SM Higgs via the usual portal interaction term. We will elaborate on the constraints on both mixing terms in a subsequent discussion.

2.1 The Higgs sector

The scalar potential is given by,

$$V(\varphi, H) = \mu_H^2 H^\dagger H + \mu_\phi^2 \varphi^\dagger \varphi + \frac{\lambda_H}{4} \left(H^\dagger H \right)^2 + \frac{\lambda_\varphi}{4} \left(\varphi^\dagger \varphi \right)^2 + \frac{\lambda_{\text{mix}}}{4} \left(H^\dagger H \right) \left(\varphi^\dagger \varphi \right) \tag{2.4}$$

The stability conditions can be read off as follows:

$$\lambda_H > 0, \ \lambda_\varphi > 0, \ \lambda_{\text{mix}}^2 < 4\lambda_H \lambda_\varphi \tag{2.5}$$

Since $\mathcal{G}_{\text{SM}} \times \text{U}(1)_D$ is broken spontaneously, we require $\mu_H^2 < 0$ and $\mu_\varphi^2 < 0$. Let v_h and v_φ denote the *vev*s of the scalar fields responsible for the spontaneous breaking of

$\mathcal{G}_{\text{SM}} \times \text{U}(1)_D$.[8] Around the minimum of the scalar potential, these scalar fields can be described as,

$$\varphi = \frac{1}{\sqrt{2}}(v_\varphi + \varphi_R + i\varphi_I) \tag{2.6}$$

and

$$H = \begin{pmatrix} \frac{1}{\sqrt{2}}\sigma_+ \\ \frac{1}{\sqrt{2}}(v_h + h + i\sigma), \end{pmatrix} \tag{2.7}$$

Here, φ_R (φ_I) and h (σ) are the CP-even (CP-odd) parts of ϕ and H respectively and σ_+ is a complex scalar. In the unitary gauge, where the low energy degrees of freedom ($d.o.f$) constitutes only the physical fields, the form of the corresponding expressions may simply be obtained by setting φ_I, σ_+ and σ to 0 in equations (2.6) and (2.7).

The squared mass matrix for the scalar fields, in the basis $\{\varphi_R, h\}$, is given by,

$$\mathcal{M}_s^2 = \begin{pmatrix} v_\varphi^2 \lambda_\varphi & v_h v_\varphi \dfrac{\lambda_{\text{mix}}}{2} \\ v_h v_\varphi \dfrac{\lambda_{\text{mix}}}{2} & v_h^2 \lambda_H, \end{pmatrix} \tag{2.8}$$

The orthonormal mixing matrix $\mathcal{N}_s$, is then given by,

$$\mathcal{N}_s = \begin{pmatrix} \cos\theta & \sin\theta \\ -\sin\theta & \cos\theta \end{pmatrix}, \tag{2.9}$$

where

$$\theta_{\text{mix}} = \frac{1}{2}\sin^{-1}\frac{v_\varphi v_h \lambda_{\text{mix}}}{(v_h^4 \lambda_H^2 + v_\varphi^4 \lambda_\varphi^2 + v_h^2 v_\varphi^2 (\lambda_{\text{mix}}^2 - 2\lambda_H \lambda_\varphi))^{\frac{1}{2}}}. \tag{2.10}$$

The mass eigenvalues can simply be obtained as the elements of the diagonal matrix $(\mathcal{M}_s^D)^2 = \mathcal{N}_s^T \mathcal{M}_s^2 \mathcal{N}_s$ and the corresponding eigenvalues give the physical masses of the CP-even neutral scalar particles,

$$M_{H_1,H_2}^2 = \frac{1}{4}\{v_h^2 \lambda_H + v_\varphi^2 \lambda_\varphi \mp (v_h^4 \lambda_H^2 + v\varphi^4 \lambda_\varphi^2 + v_h^2 v_\varphi^2 (\lambda_{\text{mix}}^2 - 2\lambda_H \lambda_\varphi))^{\frac{1}{2}}\} \tag{2.11}$$

The mass eigenstates are given by,

$$\{H_1, H_2\}^T = \mathcal{N}_s^T \{\varphi_R, h\}^T, \tag{2.12}$$

or more explicitly,

$$H_1 = \cos\theta_{\text{mix}}\ \varphi_R - \sin\theta_{\text{mix}}\ h, \tag{2.13}$$

$$H_2 = \sin\theta_{\text{mix}}\ \varphi_R + \cos\theta_{\text{mix}}\ h. \tag{2.14}$$

We will denote the mass eigenstate corresponding to the lightest eigenvalue M_{H_1} as H_1 and that to the heavier one (M_{H_2}) as H_2. In this convention $\cos\theta_{\text{mix}}$ simply denotes the φ_R content in the lightest mass eigenstate. As we will consider a scenario with a light H_1, H_2 would be the SM-like Higgs boson. Therefore, $\cos\theta_{\text{mix}}$ denotes the SM Higgs content in H_2 as well as φ_R content in H_1.

---

[8]Note that while v_φ, in general, may be complex; its phase is not physical and can be absorbed by suitable field redefinitions both in the Higgs sector and in the Dark Sector, as may be evident from the lagrangian. Therefore, v_φ has been assumed to be real.

2.2 The gauge boson sector

The gauge group in the present context is: $\mathcal{G}_{\mathrm{SM}} \times \mathrm{U}(1)_D$, where $\mathcal{G}_{\mathrm{SM}}$ denotes the SM gauge group. In this section we focus on the electroweak gauge bosons and implication of the gauge kinetic mixing with the $\mathrm{U}(1)_D$ gauge boson. The relevant lagrangian for the neutral gauge boson sector is given by,

$$\mathcal{L}_{\mathrm{gauge}} = \mathcal{L}_{\mathrm{kin}} + \mathcal{L}_{\mathrm{mass}} + \mathcal{L}_{\mathrm{int}} \tag{2.15}$$

where,

$$\begin{aligned}
\mathcal{L}_{\mathrm{kin}} &= -\frac{1}{4}\hat{W}^3_{\mu\nu}\hat{W}^{\mu\nu}_3 - \frac{1}{4}\hat{B}_{\mu\nu}\hat{B}^{\mu\nu} - \frac{1}{4}\hat{Z}_{D\mu\nu}\hat{Z}^{\mu\nu}_D + \frac{\epsilon_g}{2}\hat{B}_{\mu\nu}\hat{Z}^{\mu\nu}_D \\
&= -\frac{1}{4}\hat{V}^T_{a\mu\nu}\mathcal{K}^a_{\mathrm{V}}\hat{V}^{\mu\nu}_a
\end{aligned} \tag{2.16}$$

$$\begin{aligned}
\mathcal{L}_{\mathrm{mass}} &= -\frac{1}{2}\left(m_w\hat{W}^3_\mu - m_B\hat{B}_\mu\right)\left(m_w\hat{W}^\mu_3 - m_B\hat{B}^\mu\right) - \frac{m^2_D}{2}\hat{Z}_{D\mu}\hat{Z}^\mu_D \\
&= -\frac{1}{2}\hat{V}^T_\mu\mathcal{M}^a_{\mathrm{V}}\hat{V}^\mu.
\end{aligned} \tag{2.17}$$

The above equations are written in the (non-canonically normalized) basis, $\hat{V}_\mu = (\hat{W}^3_\mu\ \hat{B}_\mu\ \hat{Z}_{D\mu})^T$. Further,

$$\mathcal{K}^a_{\mathrm{V}} = \begin{pmatrix} 1 & 0 & 0 \\ 0 & 1 & \epsilon_g \\ 0 & \epsilon_g & 1 \end{pmatrix}, \quad \mathcal{M}^a_{\mathrm{V}} = \begin{pmatrix} m^2_w & -m_w m_B & 0 \\ -m_w m_B & m^2_B & 0 \\ 0 & 0 & m^2_D \end{pmatrix}. \tag{2.18}$$

where $m_w = \frac{g_2 v}{2}$, $m_B = \frac{g_1 v}{2}$. The kinetic term is canonical in the basis $V_\mu = \zeta\hat{V}_\mu$, with

$$\zeta = \begin{pmatrix} 1 & 0 & 0 \\ 0 & 1 - \dfrac{\epsilon^2_g}{8} & \dfrac{\epsilon_g}{2} \\ 0 & \dfrac{\epsilon_g}{2} & 1 - \dfrac{\epsilon^2_g}{8} \end{pmatrix}, \tag{2.19}$$

where we have kept only terms upto $\mathcal{O}(\epsilon^2_g)$. The invariance of the gauge covariant derivatives imply that the gauge couplings $\mathcal{G}$ in the modified basis are given by,

$$\mathcal{G} = \hat{\mathcal{G}}.\zeta^{-1} = \begin{pmatrix} \hat{g}_2 & 0 & 0 \\ 0 & \hat{g}_1\left(1 - \dfrac{3\epsilon^2_g}{8}\right) & g_{1D} \\ 0 & g_{D1} & \hat{g}_D\left(1 - \dfrac{3\epsilon^2_g}{8}\right) \end{pmatrix}, \tag{2.20}$$

where $g_{D1} = \hat{g}_D\dfrac{\epsilon_g}{2}$ and $\hat{g}_{1D} = g_1\dfrac{\epsilon_g}{2}$, and $\hat{\mathcal{G}} = Diagonal(g_2, g_1, g_D)$. In this basis, the mass matrix takes the following form,

$$\mathcal{M}^b_V = \zeta^{-1T}\mathcal{M}^a_V\zeta^{-1} \tag{2.21}$$

In this context, we have used the approach described in refs [72, 73]. We have used SARAH and SPheno [74, 75] to numerically diagonalize the mass matrix and thus obtain the respective mass eigenstates and the corresponding mixing matrix. The mass eigenstates include a zero mass state, corresponding to the unbroken electro-magnetic gauge group U(1), and two massive states representing Z and Z_D bosons respectively. Needless to mention, the mass of the Z boson, and the electroweak precision data in general, constraints ϵ_g [76, 77]. For the present work, we will mainly consider small enough ϵ_g only ensuring prompt decay of Z_D at high energy colliders.

2.3 The dark sector

After electroweak symmetry breaking (EWSB), φ_R assumes a *vev* (v_φ) generating a Majorana mass term in the dark fermionic sector. The mass term for the fermions, then, can be expressed as:

$$- \mathcal{L}_{\text{mass}} = \frac{1}{2} \{ \bar{\bar{\xi}}_1 \ \bar{\bar{\xi}}_2 \} \mathcal{M}_{\text{DM}} \{ \xi_1 \ \xi_2 \}^T + \text{h.c.} \tag{2.22}$$

where

$$\mathcal{M}_{\text{DM}} = \begin{pmatrix} fv_\varphi & M \\ M & fv_\varphi \end{pmatrix}. \tag{2.23}$$

This mass matrix can be diagonalized by an orthonormal matrix

$$\mathcal{N}_{\text{DM}} = \frac{1}{\sqrt{2}} \begin{pmatrix} -1 & 1 \\ 1 & 1 \end{pmatrix}. \tag{2.24}$$

The mass of the physical states can be obtained from the eigenvalues of $\mathcal{M}_{\text{DM}}$ and are given by $M_\pm = |M \pm fv_\varphi|$. The corresponding physical states (mass eigenstates) are $\chi_\pm = \frac{\chi^c \pm \chi}{\sqrt{2}}$. The state with the lower mass i.e. M_- is our dark matter candidate and from now on its mass will be denoted by M_{DM} for definiteness.[9]

The lagrangian $\mathcal{L}_{\text{DS}}$, in the mass basis, is given by:

$$\mathcal{L} = \frac{1}{2} \left(i\overline{\chi}_+ \gamma^\mu \partial_\mu \chi_+ + i\overline{\chi}_- \gamma^\mu \partial_\mu \chi_- - g_D Z_D^\mu \overline{\chi}_+ \gamma_\mu \chi_- - g_D Z_D^\mu \bar{\chi}_- \gamma_\mu \chi_+ \right) \tag{2.25}$$
$$- \frac{1}{2} \left(M_+ \overline{\chi}_+ \chi_+ - M_- \overline{\chi}_- \chi_- \right) - \frac{f}{2} \left((\cos\theta \, H_1 + \sin\theta \, H_2)(\overline{\chi}_+ \chi_+ - \overline{\chi}_- \chi_-) \right).$$

In the above expression, H_1 and H_2 denote the φ_R-like and h-like states (only true for small mixing), respectively, in the mass eigenbasis as discussed before.

3 Self-interaction of dark matter: allowed regions

A study of self-interaction in our dark matter scenario can give rise to novel features and lead to interesting results. As was discussed in the introduction, strongly self-interacting

---

[9] Note that we have used the absolute value of the smallest eigenvalue, since the sign of the fermion mass can simply be rotated away by a chiral rotation. For example, with $M > fv_\varphi$ and $M > 0$, the smallest eigenvalue $M - fv_\varphi$ is positive. The corresponding mass eigenstate is $\frac{1}{\sqrt{2}} \left((\xi_1 - \xi_2) \ (-\tilde{\xi}_1 + \tilde{\xi}_2) \right)^T = \gamma_5 \frac{\chi^c - \chi}{\sqrt{2}}$.

dark matter can help to alleviate many small scale structure problems. In our model there are two Majorana fermions, an extra gauge boson and an extra Higgs boson. Hence, it is generic to any such U(1) gauge theories to have vertices like $\chi_+\chi_+H_1$, $\chi_-\chi_-H_1$ and $\chi_+\chi_-Z_D$.

Here, the new gauge boson is not charged under the Standard Model gauge group. Hence it can be very light in principle. The new Higgs boson can also be quite light. A remarkable consequence of this is the Sommerfeld enhancement in the limit when $M_{DM} \gg M_{H_1}$ or M_{Z_D}, where M_{DM}, M_{H_1} and M_{Z_D} are the masses of the DM, light Higgs and the extra gauge boson. Depending on the mass of the mediator we can have the following three cases:

- When M_{H_1} is much lighter than the dark matter mass, but M_{Z_D} is heavier. Sommerfeld enhancement takes place by exchanging the light Higgs boson only by the usual ladder diagrams.

- When Z_D is lighter than the new Higgs, then enhancement proceeds by exchanging only this light extra gauge boson.

- When both Z_D and the new Higgs are of comparable masses then enhancement should in principle occur due to both the mediators.

The case when both the new gauge boson and the extra Higgs are very light may be interesting from a theoretical point of view. But, by making both of these particles light (lighter than the DM) simultaneously, we will lose out on the robust collider signatures that we also intend to explore in this work. So we do not probe those parameter regions where both of the mediators are light.

Next, let us discuss about the second case. Since the new scalar is not very light, this implies that $\lambda_{\mathrm{mix}} v_D$ is not small (from the expression of the mass of the new scalar). But on the other hand, we demand that $M_{Z_D} \sim g_D v_D$ should be much smaller than that of M_{H_1}. To satisfy both of these conditions we have to take resort to very small dark gauge boson couplings. But the enhancement factor also depends on g_D (through $\chi_+\chi_-Z_D$ vertices). Hence in this case, the enhancement that we were expecting by introducing light gauge boson mediator is nullified by the presence of small gauge couplings. So, practically speaking, Sommerfeld enhancement with only light Z_D is not a good a choice either.

Following these two points of view, we consider the first case as our preferred choice for studying strong self-interactions of dark matters.

In calculating the self-interacting cross-section we closely followed the analytical expressions presented in [66]. In the Born limit ($\alpha_D M_{DM}/M_{H_1} \ll 1$), the cross-section is given by:

$$\sigma_T^{\mathrm{Born}} = \frac{8\pi\alpha_D^2}{M_{DM}^2 v^4}\left(\log\left(1 + M_{DM}^2 v^2/M_{H_1}^2\right) - \frac{M_{DM}^2 v^2}{M_{H_1}^2 + M_{DM}^2 v^2}\right), \qquad (3.1)$$

where, $\alpha_D = f^2/4\pi$ and v is the virial velocity of galaxies.

Outside the Born regime ($\alpha_D M_{DM}/M_{H_1} \gtrsim 1$) non-perturbative effects become important. Analytical results can be obtained in the classical limit ($M_{DM}v/M_{H_1} \gg 1$). For an attractive potential [66, 78, 79]:

$$\sigma_T^{\text{clas}} = \begin{cases} \frac{4\pi}{M_{H_1}^2}\beta^2 \ln\left(1 + \beta^{-1}\right) & \beta \lesssim 10^{-1} \\ \frac{8\pi}{M_{H_1}^2}\beta^2/\left(1 + 1.5\beta^{1.65}\right) & 10^{-1} \lesssim \beta \lesssim 10^3 \\ \frac{\pi}{M_{H_1}^2}\left(\ln\beta + 1 - \frac{1}{2}\ln^{-1}\beta\right)^2 & \beta \gtrsim 10^3 \end{cases} \tag{3.2}$$

where $\beta \equiv 2\alpha_D M_{H_1}/(M_{DM}v^2)$. Analytical results can also be obtained in the resonance region in between by approximating the Yukawa potential by *Hulthen* potential [80].

$$\sigma_T^{\text{Hulthén}} = \frac{16\pi}{M_{DM}^2 v^2} \sin^2\delta_0 \tag{3.3}$$

where the $l = 0$ phase shift is given in terms of the Γ-function by

$$\delta_0 = \arg\left(\frac{i\,\Gamma\left(\frac{iM_{DM}v}{\kappa M_{H_1}}\right)}{\Gamma(\lambda_+)\Gamma(\lambda_-)}\right) \tag{3.4}$$
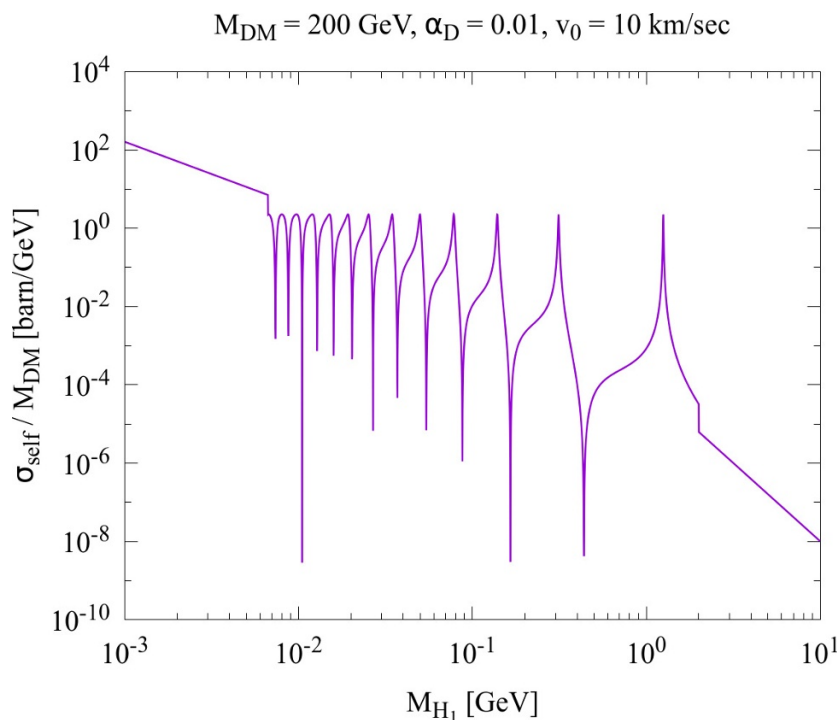
with

$$\lambda_\pm \equiv 1 + \frac{iM_{DM}v}{2\kappa M_{H_1}} \pm \sqrt{\frac{\alpha_D M_{DM}}{\kappa M_{H_1}} - \frac{M_{DM}^2 v^2}{4\kappa^2 M_{H_1}^2}} \tag{3.5}$$

and $\kappa \approx 1.6$ is a dimensionless number. The bound on self-interacting dark matter is given in terms of $\sigma_{\text{self}}/M_{DM}$. This should be $\lesssim (0.1 - 10)$ cm^2 gm^{-1} when $v_0 \sim 10$ km/sec to alleviate the *Core-vs-cusp* problem of the dwarf spheroidal galaxies [81, 82]. From the X-ray and the lensing observations of Bullet cluster we further have $\sigma_{\text{self}}/M_{DM} \lesssim 1$ cm^2 gm^{-1} [58] when $v_0 = 1000$ km/sec.

The self-interaction cross-section in units of the dark matter mass (for a fixed α_D and M_{DM}) is plotted with respect to the mediator mass in figure 1. Since we are concentrating on the low mediator mass regime in this study, the mass of the light Higgs was varied up to 10 GeV throughout this work. If we now perform a scan by varying both the dark matter mass (0.1 GeV–1 TeV) and the mediator mass (0.1 MeV–10 GeV), and the allowed points (i.e. points with 0.1 cm^2 gm^{-1} $\lesssim \sigma_{\text{self}}/M_{DM} \lesssim 10$ cm^2 gm^{-1}) are plotted, then we arrive at figure 2 (left). This was however done for a fixed α_D ($\equiv f^2/4\pi$) = 0.001. The right hand panel of figure 2 shows the more general case with varying α_D. The values of α_D are shown in the colour bar. We see immediately that for light mediators (with mass reaching up to 10 GeV) and for a wide range of dark matter masses, the allowed range of α_D is quite large. Note that, self-interaction can be achieved even for very small values of α_D ($\sim 10^{-7}$) when the mediator is extremely light (~ 100 keV). Here, we have taken care of the bounds on the self-interaction cross-section arising from the Bullet Cluster.

So, to summarise, in this work we will be concentrating on self-interaction of dark matter mediated by light scalar mediators alone. But, this mediator (H_1) cannot be extremely light in order to respect the constraints arising from BBN [83, 84]. This is because, BBN

Figure 1. Sommerfeld enhancement with respect to mediator mass for a fixed dark matter mass and fixed coupling strength α_D.
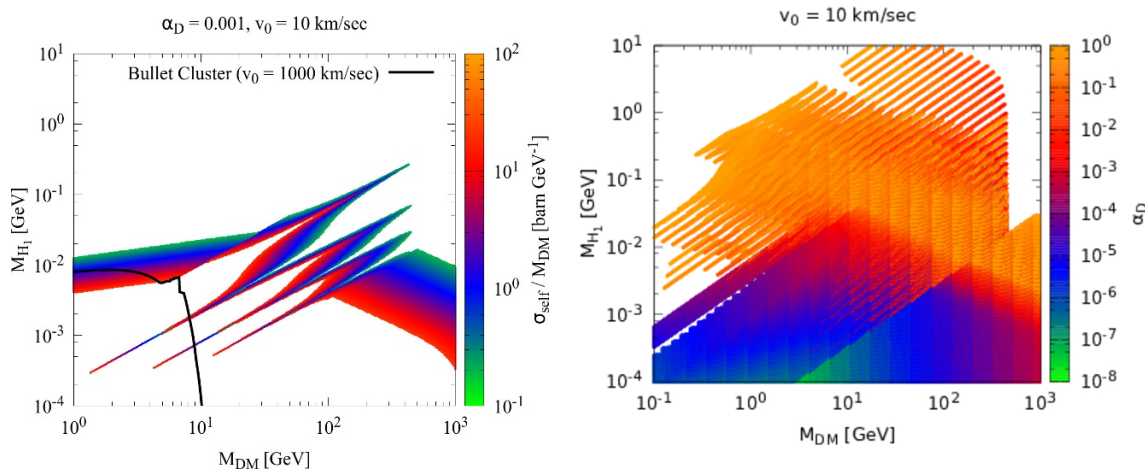
Figure 2. *Left:* region for allowed self-interaction with varying dark matter and mediator mass for a fixed α_D. v_0, the virialized velocity is fixed to 10 km/sec. The region within the black contour denotes the part of the parameter space ruled from Bullet cluster [56–58] constraint (see text for more details). *Right:* region of parameter space where moderate to strong self-interaction of dark matter is allowed to alleviate *Core-vs-cusp, Too-big-to-fail* problems, with varying α_D (0.1 cm^2 gm^{-1} $\lesssim \sigma_{\text{self}}/M_{DM} \lesssim$ 10 cm^2 gm^{-1}). The variation of α_D is shown in the color bar. The allowed points shown in this figure satisfies the constraint arising from Bullet Cluster.

places strong upper bounds on presence of relativistic particles when temperature of the universe is $\sim 1\,\mathrm{MeV}$. Hence, for all practical purposes, $M_{H_1} \gtrsim 10\,\mathrm{MeV}$ would be admissible. Therefore, the mass range of the scalar H_1 for suitable self-interaction is expected to be: $10\,\mathrm{MeV} \lesssim M_{H_1} \lesssim 10\,\mathrm{GeV}$. We will concentrate on this range of M_{H_1} throughout the rest of the work. The upper bound on self-interaction cross-section from Bullet Cluster was also taken into consideration during our calculation.

4 Survey of parameter space

The latest results from the SM Higgs coupling measurements still allow the SM Higgs to have non-standard couplings. In the context of the $\mathrm{U}(1)_D$ model considered in this work, such non-standard decay modes of the SM-like Higgs boson could arise in three possible ways, viz., decay into a pair of light Higgs bosons ($H_2 \to H_1 H_1$), decay into a pair of dark gauge bosons ($H_2 \to Z_D Z_D$) and decay into the Majorana fermions ($H_2 \to \chi_+ \chi_+, \chi_- \chi_-$). The $H_2 \to H_1 H_1$ decay width is crucially controlled by $\sin \theta_{\mathrm{mix}}$, while the $H_2 \to Z_D Z_D$ decay process also has a direct dependence on ϵ_g^2. Throughout this analysis, we restrict the mass of Z_D within $M_{Z_D} < 60$ GeV. Thus, the $H_2 \to H_1 H_1$ and $H_2 \to Z_D Z_D$ decay modes always remain kinematically feasible.

We perform a random scan over the 9-dimensional parameter space to capture the underlying physics of the $\mathrm{U}(1)_D$ model. In this respect, we scan over the following parameters: λ_H, λ_ϕ, λ_{mix}, g_D, ϵ_g, v_D, M, and f. The scan range is inspired by the region of parameter space shown in figure 2 (b) which corresponds to those sectors which facilitate a dark matter with moderate to strong self-interactions. It can be observed from figure 2 that a self-interacting DM up to mass 1 TeV could be accommodated with $M_{H_1} < 10$ GeV. The mass of H_1 (eq. 2.11) is determined by λ_ϕ, λ_{mix} and v_D, and the range of these parameters is chosen in such a way that a significant fraction of scanned points populate the $M_{H_1} \lesssim 10$ GeV region. Correspondingly, M has also been varied from 1 GeV $-$ 1000 GeV to obtain the DM mass in that range. Since we are interested in studying the collider prospects of Z_D, whose mass is given by $g_D \times v_D$, the choice of g_D is governed primarily by the requirement of M_{Z_D} within 2 GeV $-$ 60 GeV.

$$0.10 < \lambda_H < 0.16, \qquad 10^{-8} < \lambda_\phi < 0.7, \qquad 10^{-12} < \lambda_{\mathrm{mix}} < 0.3 \qquad (4.1)$$

$$10^{-6} < g_D < 0.6, \qquad 10^{-4} < \epsilon_g < 10^{-10} \qquad (4.2)$$

$$1\ \mathrm{GeV} < v_D < 1000\ \mathrm{GeV}, \qquad 10^{-6} < f < 10^{-1}, \qquad 1\ \mathrm{GeV} < M < 500\ \mathrm{GeV} \qquad (4.3)$$

5 Constraints

The $\mathrm{U}(1)_D$ parameter space discussed so far gets constrained by a multitude of experimental search results. Combined measurement of the Higgs boson mass by the ATLAS and CMS collaborations confines it within 124.4 GeV - 125.8 GeV [85] at $3\,\sigma$. Consequently, the mass of H_2 is required to lie within 124.4 GeV $< M_{H_1} < 125.8$ GeV. The parameter space points obtained by imposing the Higgs mass constraint, $M_{Z_D} < 60$ GeV and $M_{H_1} < 10$ GeV are
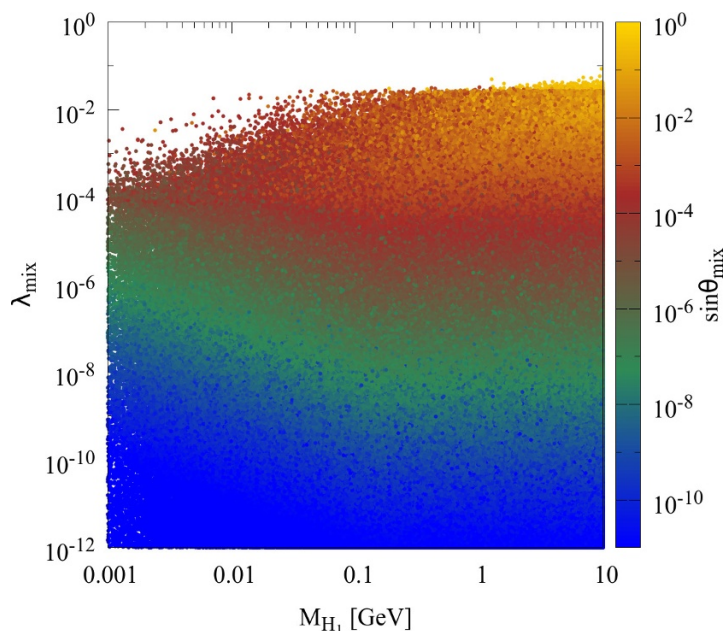
Figure 3. Parameter space points with $M_{H_1} \leq 10$ GeV, $M_{Z_D} \leq 60$ GeV and 124.4 GeV $\leq M_{H_2} \leq 125.8$ GeV, in the $M_{H_1} - \lambda_{\mathrm{mix}}$ plane with $\sin\theta_{\mathrm{mix}}$ presented in the color palette.

shown in figure 3 in the $\lambda_{\mathrm{mix}} - M_{H_1}$ plane. The color palette represents the value of $\sin\theta_{\mathrm{mix}}$, and exhibits its direct proportionality with λ_{mix}.

The effect of constraints on $\sin\theta_{\mathrm{mix}}$ from light H_1 searches at LEP has been analyzed in this section. We also evaluate the implications from Higgs signal strength measurements through a global χ^2 analysis, by combining, both, 8 and 13 TeV LHC results. The status of our parameter space in light of direct Z_D searches at the LHC is studied as well. The $U(1)_D$ parameter space under study also receives strong constraints from measurements at B-factories and various beam dump experiments. In the remainder of this section, we will analyse in detail, the implications on our parameter space from each of these constraints.

5.1 Constraints from LEP

The two LEP collaborations, DELPHI and OPAL, have performed numerous searches for the Higgs boson using data collected from e^+e^- collisions at $\sqrt{s}$ ranging from ~ 91 GeV $-$ 209 GeV, with no observation of signal like events. DELPHI has performed searches for light H_1 using the $e^+e^- \to ZH_1 \to (Z \to e^+e^-, \mu^+\mu^-)H_1$ [88] and $Z \to e^+e^-$, $\mu^+\mu^-$, $\tau^+\tau^-$, $\nu\bar{\nu}$, $q\bar{q}$ [89] processes. The di-Higgs $(e^+e^- \to H_2H_1)$ and triple Higgs $(e^+e^- \to H_2H_1 \to H_1H_1H_1)$ final states have also been analyzed by LEP in 4τ, $4b$, $2b2\tau$, 6τ, $6b$ channel [90].

Upper bounds on $H_1VV(V = W^\pm, Z)$ coupling normalized to that for SM, at 95% C.L., taking into account, both, LEPI and LEPII data has been derived in [86]. In the context of our analysis, the normalized H_1VV coupling (ζ) is directly proportional to $\sin\theta_{\mathrm{mix}}$, and the upper limits derived in [86] exclude the blue colored points in figure 4, corresponding to $\sin\theta_{\mathrm{mix}} \gtrsim 0.5$, for the entire range of M_{H_1} obtained in our parameter space scan. A
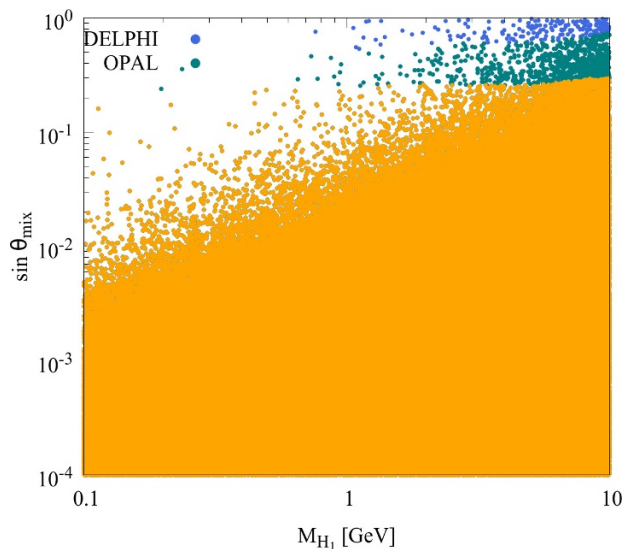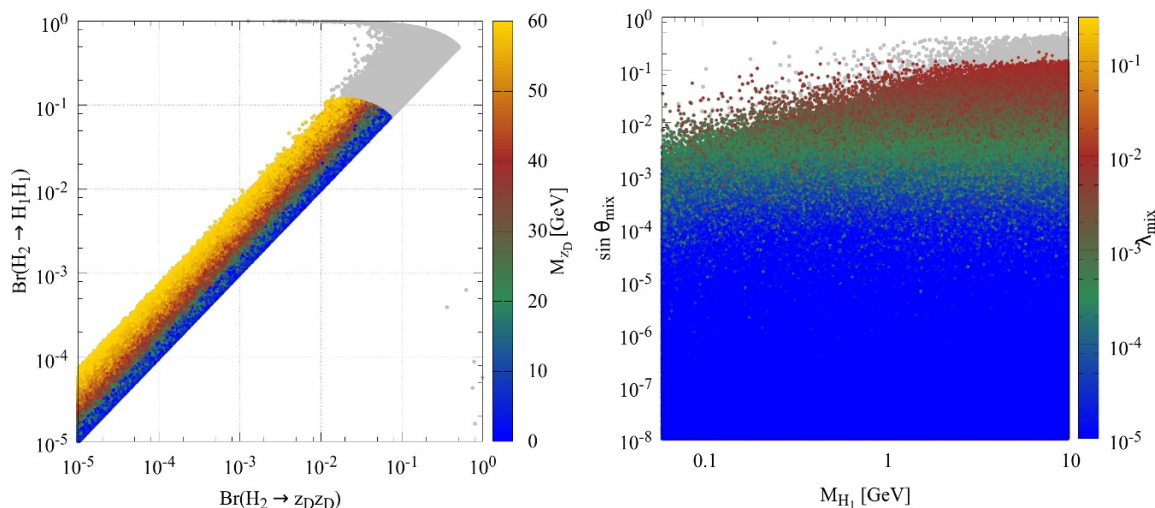
Figure 4. Scatter plot in the M_{H_1} - $\sin\theta_{\mathrm{mix}}$ plane showing the implications of imposing the LEP constraints on our parameter space. All parameter space points satisfy the Higgs mass constraints and have $M_{H_1} < 10$ GeV and $M_{Z_D} < 60$ GeV. The blue colored parameter space points are ruled out by upper limits derived on ζ^2 by DELPHI [86], where ζ is the normalized $H_1 VV$ coupling with respect to SM. The green colored points are excluded by the upper limits on κ derived by OPAL [87], where κ is the ratio of production cross-section of H_1 in the Higgs strahlung process to its SM value. The yellow colored points represents the allowed region of parameter space.

study by OPAL collaboration [87], using the LEPI and LEPII dataset, has derived upper bounds on κ at 95% C.L., for $M_{H_1} = 10^{-6} - 100$ GeV, where κ is the ratio of production cross-section of the new light scalar in the Higgs strahlung process to that of SM Higgs production in the Higgs strahlung process, under the assumption that the mass of the new light scalar is equal to the SM Higgs. Within the U(1)$_D$ model considered here, κ is proportional to $\sin^2\theta_{\mathrm{mix}}$, and the corresponding upper bounds, upon being implemented on our parameter space, excludes the green colored region in figure 4. We find that the upper limits from [87] exerts a relatively stronger constraint on the parameter space and excludes $\sin\theta_{\mathrm{mix}} \gtrsim 0.2$, over the entire range of M_{H_1}[10] obtained in our parameter space scan.

5.2 Constraints from LHC Higgs signal strength measurements

The ATLAS and CMS collaborations have performed numerous measurements of the coupling of the 125 GeV Higgs boson using LHC Run-I and Run-II datasets. Results from these measurements are usually presented through signal strength observables, which considers

---

[10]It may be noted that decay channels originating from the light scalar Higgs ($M_{H_1} \lesssim 2$ GeV) require a careful treatment owing to the uncertainties associated with partial decay widths of H_1 into hadronic channels. Within $2m_\pi \lesssim M_{H_1} \lesssim 2$ GeV, the uncertainties associated with theoretical calculations remain significant [91] (in the second printing (1990) by Perseus Books in the collection Frontiers in physics, no. 80, a number of errors and omissions are corrected and the references at the end of each chapter are updated. A paperback reprint of the 1990 edition has been published in 2000), and the corresponding partial decay widths are computed using low energy effective theories of QCD. In our analysis, we have considered the branching ratios of $H_1 \to \gamma\gamma$, e^+e^-, $\mu^+\mu^-$ from [92].

Figure 5. The grey colored points are excluded by the global χ^2 analysis. *Left:* correlation between $Br(H_2 \to H_1 H_1)$ and $Br(H_2 \to Z_D Z_D)$. The color palette represents the value of M_{Z_D}. *Right:* scatter plot in the M_{H_1} - $\sin \theta_{\mathrm{mix}}$ plane. The color palette represents the value of λ_{mix}. The grey colored points are excluded by the signal strength constraints.

the most important Higgs production modes at LHC: gluon fusion mode (ggF), vector boson fusion (VBF), associated production with vector bosons (VH_2, $V = W^{\pm}, Z$) and associated production with a top-antitop pair ($t\bar{t}h$), and the relevant Higgs boson decay modes: $H_2 \to b\bar{b}$, $\tau^+\tau^-$, WW, ZZ, $\gamma\gamma$. The signal strength variable is defined as

$$\mu = \frac{(\sigma_{H_2}^i \times Br_{H_2}^j)_{\mathrm{Model}}}{(\sigma_{H_2}^i \times Br_{H_2}^j)_{\mathrm{SM}}} \tag{5.1}$$

Here, $\sigma_{H_2}^i$ corresponds to the Higgs production cross-section in the ith mode ($i = ggF$, VBF, VH_2 and $t\bar{t}H_2$), and $Br_{H_2}^j$ corresponds to the branching fraction of the Higgs in the jth decay mode ($j = b\bar{b}$, $\tau^+\tau^-$, WW, ZZ, $\gamma\gamma$). $(\sigma_{H_2}^i)_{\mathrm{SM}}$ and $(Br_{H_2}^i)_{\mathrm{SM}}$ corresponds to the SM counterparts. In the current analysis, the heavier scalar Higgs boson, H_2, is required to be consistent with the SM 125 GeV Higgs boson, thereby requiring it to be dominantly doublet-like. However, mixing between the doublet and singlet Higgs fields renders a small singlet admixture in H_2 as well. The coupling of H_2 with the SM particles remain similar to that of the case of SM Higgs boson, except for an additional suppression (by $\cos \theta_{\mathrm{mix}}$). Consequently, the $t\bar{t}H_2$ vertex in the ggF production mode of Higgs, and the VVH_2 vertex in the VBF, VH_2 and $t\bar{t}H_2$ production modes of Higgs, gets an additional factor of $\cos \theta_{\mathrm{mix}}$, resulting in the Higgs production cross-section acquiring a $\cos^2 \theta_{\mathrm{mix}}$ suppression. As a result, the ratio of $\sigma_{H_2\,\mathrm{Model}}^i / \sigma_{H_2\,\mathrm{SM}}$ in eq. (5.1) can be approximated to $\cos^2 \theta_{\mathrm{mix}}$. The branching fraction of H_2 to SM final states also gets affected by the presence of new non-SM decay modes. As specified in the previous section, H_2 has three possible non-SM decay modes, and the relative interplay of input parameters determine the partial decay width in each of the SM channel.

In this study, the signal strength constraints have been imposed upon the scanned parameter set through a global χ^2 analysis,[11] performed by taking into account the most recent Higgs signal strength constraints, tabulated in table II and table III of [94]. The value of χ^2 is computed as

$$\chi^2 = \Sigma_i \frac{(\bar{x}_i - x_i)^2}{\Delta x_i^2} \tag{5.2}$$

where, x_i corresponds to the best-fit value of the observable derived through experimental measurements, $\bar{x}_i$ corresponds to the value of the observable computed for the current model, and Δx_i refers to the error associated with the experimental measurement. In the context of this study, x_i represents the best-fit value of the signal strength observables. The value of χ^2 was computed for all scanned parameter space points by combining 28 signal strength observables from LHC Run-I data and 18 observables from LHC Run-II data ($\sim 15\, fb^{-1}$ and $\sim 36\, fb^{-1}$),[12] and the lowest value of χ^2 was determined (represented by $\chi^2_{\min}$). Allowing 2σ uncertainty, we choose parameter space points which lie within $\chi^2_{\min} + 6.18$. The implications of the global χ^2 analysis are shown in figure 5. We would like to note that the parameter space points corresponding to figure 5 (left) have been generated from the parameter space specified in eq. (4.3), except for f ($f \simeq 0.1$) and M ($M \simeq 500$ GeV). Thus, $H_2 \to H_1 H_1$ and $H_2 \to Z_D Z_D$ are the only non-SM decay modes for H_2. We show the correlation between these two non-SM decay modes in figure 5 (left), where the grey points (color palette points) have been excluded (allowed) by the global χ^2 analysis. The $H_2 Z_D Z_D$ coupling emerges from the $D_\mu \phi^\dagger D^\mu \phi$ term, when one of the singlet Higgs field receives a vacuum expectation value. The covariant derivative contains a term $\propto g_D Z_D$, and the ϕ field yields a term proportional to $\sin\theta_{\mathrm{mix}} H_2$, resulting in the $H_2 Z_D Z_D$ coupling to become proportional to $g_D^2 \times \sin\theta_{\mathrm{mix}}$. Another contribution arises from the SM term $D_\mu H^\dagger D^\mu H$ through $Z - Z_D$ mixing. However, this term is proportional to ϵ_g^2 and since we have restricted ourselves to small values of ϵ_g, contributions from this term can be safely ignored. The $H_2 H_1 H_1$ coupling manifests from the quadratic Higgs mixing term in the scalar potential, $\frac{\lambda_{\mathrm{mix}}}{4}(H^+ H)(\phi^\dagger \phi)$, and is therefore, proportional to $\lambda_{\mathrm{mix}} v_H$. It can be observed from figure 5 (left) that the current constraints from Higgs signal strength measurements allow the SM-like Higgs (H_2) to have $\lesssim 15\%$ of non-SM branching fraction. In the low ϵ_g limit, ratio of $Br(H_2 \to H_1 H_1)$ to $Br(H_2 \to Z_D Z_D)$ is directly proportional to M_{Z_D}, and the same can be visualized in figure 5 (left), where the color palette represents the value of M_{Z_D}.

In figure 5 (right), we show the parameter space points allowed by the global χ^2 analysis (color palette points) in the $M_{H_1} - \sin\theta_{\mathrm{mix}}$ plane, while the points excluded by the same have been shown in grey color. The generic parameter space of eq. (4.3) has been represented in figure 5 (right). Within this scenario, H_2 can also decay into the additional non-SM decay mode: $H_2 \to DM\ DM$, depending on the values of f and M. It can be visualized from figure 5 (right) that the signal strength constraints wield an approximately flat exclusion on $\sin\theta_{\mathrm{mix}} \gtrsim 0.1$ over the entire range of H_1 mass. Hence limits on $\sin\theta_{\mathrm{mix}}$
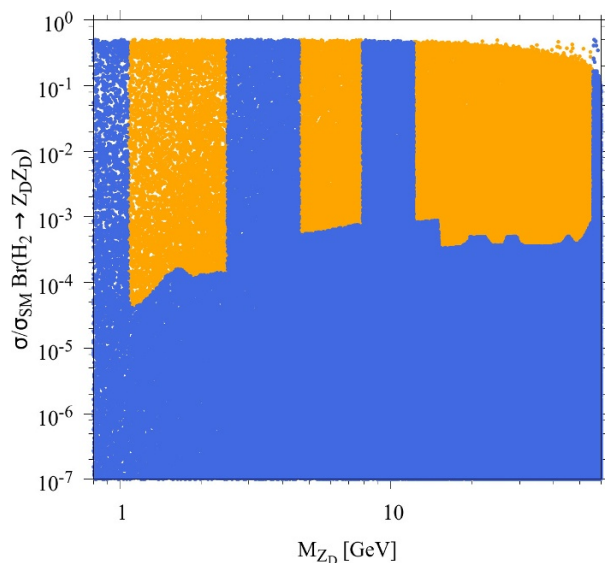
---

[11]This analysis set up has been validated in [93, 94].

[12]For details see table II and III of [94].
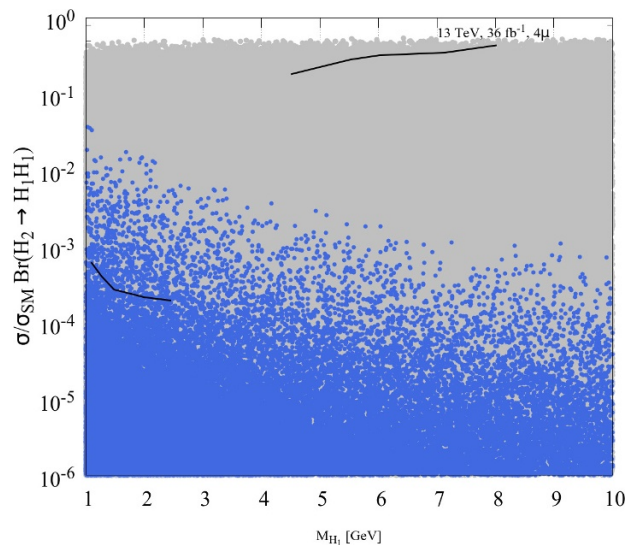
Figure 6. Scatter plot showing $\sigma_{H_2}/\sigma_{H_{\mathrm{SM}}} \times Br(H_2 \to H_1 H_1)$ vs M_{H_1} for the allowed parameter space points. The solid black line represents the upper limit on $\sigma_{H_2}/\sigma_{H_{\mathrm{SM}}} \times Br(H_2 \to AA)$ derived by ATLAS from search in the 4μ final state, using the LHC Run-II dataset corresponding to $\sim 36.1 \ fb^{-1}$ [95].

Figure 7. Scatter plot in the $M_{Z_D} - \sigma/\sigma_{\mathrm{SM}} \times Br(H_2 \to Z_D Z_D)$ plane exhibiting the implications from application of upper limits derived by LHC from search in the $H_2 \to Z_D Z_D \to 4l$ channel [95]. All parameter space points in this figure satisfy the Higgs mass constraints. The blue colored points are the ones which are still allowed by the $H_2 \to Z_D Z_D$ search limits.

from LHC signal strength measurements are two times stronger compared to the results from LEP (shown in figure 4).

5.3 Constraints from LHC direct searches

ATLAS and CMS have performed different searches for the Higgs boson with a mass of 125 GeV decaying into two spin-zero particles, $H_2 \to AA(SS)$, in various final state using Run-I and Run-II datasets. The ATLAS collaboration has analysed the $4l$ $(l = e, \mu)$ final state originating from the decay of 125 GeV Higgs boson via an intermediate ZZ_D, Z_DZ_D and AA pair production using the 13 TeV dataset collected at $\mathcal{L} \sim 36.1$ fb^{-1} [95]. This search probed the mass range of 1 GeV $\leq M_A \leq$ 60 GeV, and furnishes the strongest bounds for lower values of M_A or M_{H_1} (in the range 1 to 8 GeV). We show these limits as a solid black colored line in figure 6, where the allowed parameter space points have been plotted in the $\sigma_{H_2}/\sigma_{H_{SM}} \times Br(H_2 \to H_1H_1)$ plane. It can be observed that the current LHC limit excludes a fraction of our parameter space points in the low H_1 mass region, $M_{H_1} \lesssim 2.5$ GeV, however, it would require an improvement of roughly ~ 3 orders of magnitude in order to become sensitive enough for the $M_{H_1} \gtrsim 4$ GeV region. The ~ 36 fb^{-1} dataset was also used by ATLAS to probe the $2b2\mu$ final state produced via $H_{SM} \to SS \to 2b2\mu$ [96] and $4b$ final state originating via $H_{SM} \to SS \to 4b$ [97], where S is a spin-zero boson, in the mass range 18 GeV $< M_S <$ 62 GeV. The CMS collaboration has also searched the 4μ final state produced via $H_{SM} \to SS \to 4\mu$, and derived upper limits in the mass range 0.25 GeV $< M_S <$ 8.5 GeV. This search used the 13 TeV dataset collected at $\mathcal{L} \sim 35.9$ fb^{-1} [98]. The same dataset has also been used by CMS to search for exotic decays of the Higgs boson to a pair of light A in the $2b2\tau$ [99] and $2\mu2\tau$ [100] final state, focussing on the mass range 15 GeV $< M_A <$ 62 GeV. ATLAS and CMS have also performed similar searches using the LHC Run-I dataset for a multitude of final states: 4τ [101], $2\mu2b$ [101], $2\mu2\tau$ [101, 102], 4μ [103, 104], 4τ [105, 106], $2\tau2b$ [107].

The ATLAS collaboration has searched for the dark vector boson (Z_D) in the mass range of 1 GeV $\lesssim M_{Z_D} \lesssim$ 60 GeV, where Z_D can be produced as pair (Z_DZ_D) or in association with SM Z boson and eventually the Z_DZ_D/ZZ_D pair decays into $4l(l = e, \mu)$ final state [95]. Upper limits were obtained on the quantity $\sigma/\sigma_{SM} \times Br(H_2 \to ZZ_D)$ or $\sigma/\sigma_{SM} \times Br(H_2 \to Z_DZ_D)$, where σ and σ_{SM} are the production cross-sections of the SM-like Higgs boson in the NP and SM scenarios. It is to be noted that the limits obtained in [95] assume $Br(Z_D \to e^+e^-) \sim 50\%$ and $Br(Z_D \to \mu^+\mu^-) \sim 50\%$, resulting in $4l = 4e(25\%)$, $2e2\mu(50\%)$, $4\mu(50\%)$, and therefore, a correct scaling is required while evaluating the implication of these constraints on the NP model under consideration. The decay processes: $H_2 \to ZZ_D$ and $H_2 \to Z_DZ_D$, depend on the kinetic mixing factor (ϵ_g), and are independent of the mixing between the Higgs doublet from the SM and the singlet Higgs from the dark sector. As a result, these decay channels serve an excellent probe of ϵ_g. However, in the case of $H_2 \to ZZ_D \to 4l$ search channel, the SM $H_{SM} \to ZZ^* \to 4l$ process offers a strong irreducible background, and eventually dilutes the resolution between the signal and background, rendering these search limits insensitive to the low ϵ_g region which is relevant to our parameter space. On the other hand, the search channel, $H_2 \to Z_DZ_D \to 4l$ stands on an advantageous ground owing to the possibility of application of SM Z-boson veto, which significantly improves the signal sensitivity as compared to the earlier case. We show the implications from the current Z_D limits from $H_2 \to Z_DZ_D$ searches (from [95])

on our parameter space in figure 7. The vertical axis corresponds to the $\sigma/\sigma_{\mathrm{SM}} \times Br(H_2 \to Z_D Z_D)$ and the horizontal axis corresponds to M_{Z_D}. The yellow colored points in figure 7 are excluded by the current direct search constraints while the blue colored points are still allowed. These search limits exclude $\sin\theta_{\mathrm{mix}}$ upto ~ 0.006 for $M_{Z_D} \sim 1-2$ GeV. The impact becomes less severe at $M_{Z_D} \gtrsim 4$ GeV, where $\sin\theta_{\mathrm{mix}}$ is excluded upto ~ 0.01

5.4 Constraints from B-factories and beam dump experiments

The LHCb collaboration [108] has derived upper limits on the kinetic mixing factor at 90% C.L., covering 214 MeV $\lesssim M_{Z_D} \lesssim 70$ GeV, using the LHC data set collected at an integrated luminosity of $1.6\,fb^{-1}$ at $\sqrt{s} = 13$ TeV. For $M_{Z_D} \gtrsim 10$ GeV, this search offers the strongest upper limits on ϵ_g, among all other contemporary dark photon experiments, and excludes $\epsilon_g \gtrsim 10^{-3}$ for $M_{Z_D} \sim 10.6$ GeV. The limit becomes slightly weaker towards higher M_{Z_D} and excludes $\epsilon_g \gtrsim 2 \times 10^{-2}$ at $M_{Z_D} \sim 70$ GeV. At M_{Z_D} below 10 GeV, the most stringent constraints are offered by BaBar [109], which exclude $\epsilon_g \gtrsim 10^{-3}$ in the mass range 0.25 GeV $< M_{Z_D} < 10$ GeV. BaBar performed the search in the $e^-e^+ \to Z_D\gamma$ channel, while assuming that the Z_D predominantly decays invisibly. In the current analysis, our scanned set of parameter space points have M_{Z_D} in between 2 GeV and 60 GeV, while ϵ_g has been scanned up to 10^{-4}. Thus, the current constraints on ϵ_g derived from dark vector boson searches do not affect our parameter space. In addition to the Z_D searches by LHCb and BaBar, there are numerous beam dump experiments which have also probed a light vector gauge boson. However, the searches by the beam dump experiments mostly concentrate in the mass range of the order $O(MeV)$. Some of these experiments are KLOE [110], MAMI [111], NA-64 [112], E141 [113], E774 [114], KEK [115], HADES [116], and Mini-BooNE [117]. Some of the upcoming experiments like DarkLight [118] and APEX [119], are expected to improve upon the sensitivity to ϵ_g by ~ 2 orders of magnitude.

Light scalar boson searches in B-factory and beam dump experiments also yield exclusion contours on $\sin\theta_{\mathrm{mix}}$ as a function of M_{H_1}. The E949 experiment [120] probed the kaon decay process, $K^+ \to \pi^+\nu\bar\nu$, in the pion momentum range 140 MeV $< p_\pi < 199$ MeV. These search limits have been translated to the $M_{H_1} - \sin^2\theta_{\mathrm{mix}}$ plane in [126] by reinterpreting the analysis scheme of [127]. In the context of our analysis, we use the corresponding exclusion contour shown in figure 1 of [126] and show the excluded parameter space points in purple color in figure 8. The CHARM collaboration [121] performed a search for axion like particles using a 400 GeV proton beam from CERN-SPS dumped onto a copper target. The corresponding limits have also been translated and presented as exclusion contours in the $M_{H_1} - \sin\theta_{\mathrm{mix}}$ plane in [126], which we directly use in our analysis, and the excluded parameter space points have been shown in yellow color in figure 8. We would like to note that the sensitivities of CHARM and E949 experiments overlap in the $M_{H_1} \lesssim 250$ MeV region with E949 exerting more stringent constraints below $M_{H_1} \lesssim 40$ MeV. Results from the search for weakly interacting massive particles by the SuperCDMS collaboration [122] has also been extracted from figure 1 of [126], and excludes the parameter space region corresponding to $M_{H_1} \gtrsim 5$ GeV and $\sin^2\theta_{\mathrm{mix}} \gtrsim 10^{-5}$. These excluded points have been shown in light brown color in figure 8. The B-factories exert the strongest constraints on $\sin^2\theta_{\mathrm{mix}}$ in the intermediate light Higgs mass region,
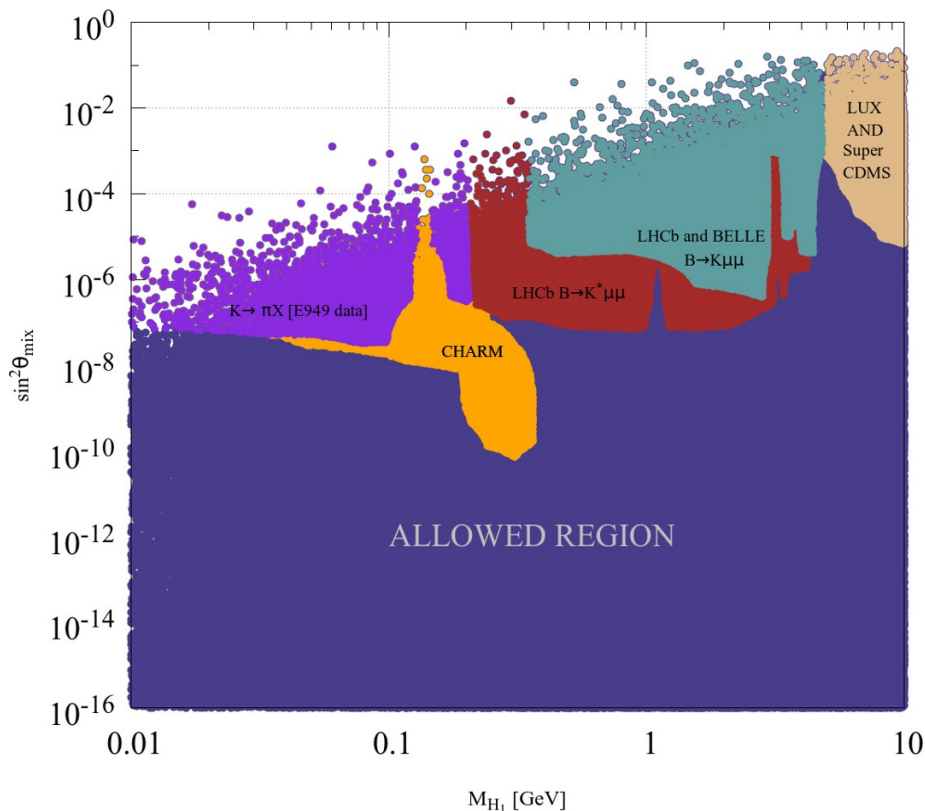
Figure 8. Summary of parameter space region excluded by the various beam dump [120–122] and flavor physics experiments [123–125].

400 MeV $\lesssim M_{H_1} \lesssim$ 5 GeV. The search for H_1 performed by LHCb collaboration [123] in the decay process: $B^0 \to K^+\pi^- H_1$, with the H_1 eventually decaying into a di-muon pair, excludes $\sin^2\theta_{\text{mix}} \gtrsim 10^{-7}$ in the mass range of 214 MeV $\lesssim M_{H_1} \lesssim$ 4 GeV. The corresponding exclusion contour has been taken from figure 1 of [126] and the excluded parameter space points have been shown in red color in figure 8. The measurements in $B \to K H_1$ channel by BELLE [124, 125] and LHCb have also been translated into limits on $\sin^2\theta_{\text{mix}}$ in [126]. The parameter space points excluded by those are shown in sky blue color in figure 8. It can be observed from figure 8 that $\sin\theta_{\text{mix}}$ values above $\sim 3 \times 10^{-3}$ are roughly excluded over the $M_{H_1} \lesssim$ 5 GeV region. The CHARM sensitivity extends out till $\sin\theta_{\text{mix}} \gtrsim 10^{-5}$ over a small range of M_{H_1}, 200 MeV $\lesssim M_{H_1} \lesssim$ 400 MeV. The parameter space points which are still allowed by the flavor physics and beam dump experiments have been shown in deep blue color.

5.5 Constraints from cosmology and astro-physics

Further, constraints on light mediators can come from Big Bang Nucleosynthesis (BBN) [84] and Cosmic Microwave Background Radiation (CMBR) [2, 128, 129]. The effect on BBN comes from mainly due to the contribution of the light mediator ($\lesssim 1\,\text{MeV}$) to the energy density at the onset of BBN, as well as from the late decay of the mediator during the BBN. For our context, we restrict the mediator mass $\gtrsim 10\,\text{MeV}$. When the decay into μ, π

are kinematically forbidden, such a mediator decays mostly into e^+e^-, and the constraints have been discussed in refs. [92, 130–133]. The effect on CMB (on the MeV mediators relevant for our context), is mainly due to the enhanced DM annihilation rate during the recombination epoch [128]. However, note that, in our case DM annihilating into a pair of light Higgs is a p-wave process, and thus, would have additional velocity suppression during the recombination epoch. Also, an abundance of the light mediator can lead to late kinetic decoupling of the DM, and thus can lead to a reduction in the small scale power, thus attracting constraints from Lyman-α observations [134–137]. The presence of light (late decaying) mediators can also enhance the rate of supernovae cooling and such particles may be constrained from the same [138].

6 Dark matter aspects

Having constrained a substantial part of the parameter space from flavor physics, beam dump and collider experiments, we now turn to dark matter phenomenology, which, as we shall see, will help us to put more stringent limits on our model thereby enhancing its predictability.

6.1 Prospects of direct detection

The direct detection experiments pose severe constraints on interactions of DM with nucleons. In the present context, we will assume H_1 to be very light, as required to enhance the self-interaction cross-section of the DM. Further, scenarios with both heavy DM and light DM (χ_-) will be discussed.

Note that, the contribution from only H_1, H_2 mediated processes are important since Z_D couples to $\chi_- - \chi_+$. Thus, if $\delta M = M_+ - M-$ is greater than $\frac{1}{2}M_- v_{\rm esc}^2$ (for $M_- \simeq \mathcal{O}(10)\,{\rm GeV}$, $\delta M \simeq \mathcal{O}(100)\,{\rm keV}$), where $v_{\rm esc} \simeq 544$ km/s denotes the escape velocity of our galaxy, the incoming DM particle (χ_-) would not have enough kinetic energy to excite the heavier state, leading to kinematic suppression of the Z_D mediated t-channel process.

The differential event-rate at a detector, as a function of the nuclear recoil energy E_R, is given by,

$$\frac{dR}{dE_R} = n_T \frac{\rho_{\chi_-}}{M_-} \int_{v_{\rm min}} d^3 v f_E(\vec{v}) v \frac{d\sigma(v, E_R)}{dE_R} \tag{6.1}$$

where, n_T is the number of target nuclei in the detector material, ρ_{χ_-} is the local density of DM halo ($\simeq 0.3 {\rm GeV cm}^{-3}$) and $\dfrac{d\sigma(v, E_R)}{dE_R}$ is the scattering cross-section with a nucleus. Further, $f_E(\vec{v})$ denotes the velocity distribution of the DM with respect to earth and can be related to the velocity distribution $f(\vec{v})$ of DM in the galactic halo as $f_E(\vec{v}) = f(\vec{v} + \vec{v}_E)$ where $\vec{v}_E$ denotes the velocity of earth in the galactic rest frame. We will assume $f(\vec{v})$ to be a Maxwell-Boltzmann distribution with velocity dispersion $v_0 = 220$ km/s and a cut-off set to $v_{\rm esc}$. The minimum velocity $v_{\rm min}$ corresponding to a recoil energy E_R is given by,

$$v_{\rm min}(E_R) = \frac{m_T E_R}{2\mu^2}, \tag{6.2}$$
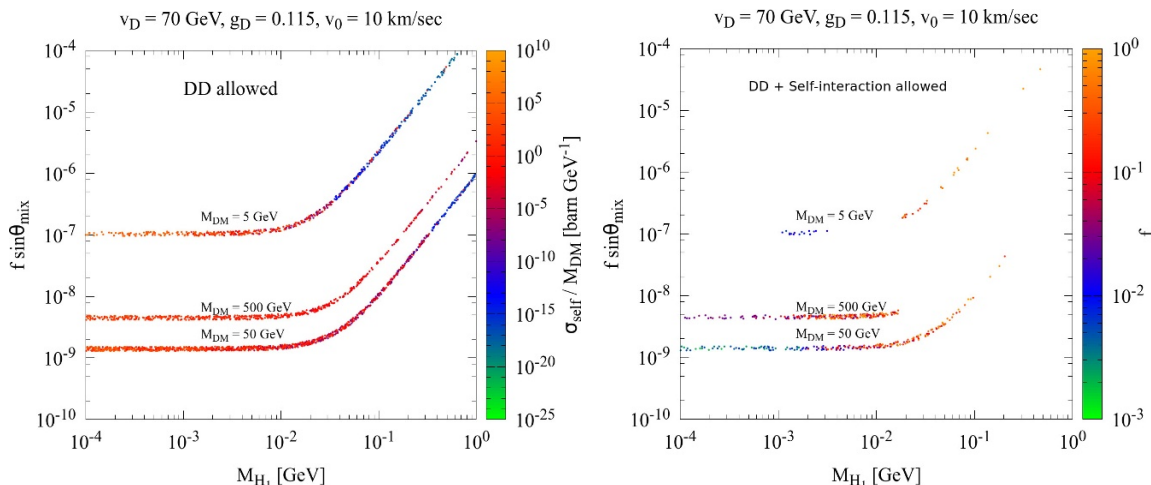
Figure 9. Constraints from direct detection experiment `Xenon-1T` [139] on $f \sin\theta_{\mathrm{mix}}$ as a function of dark scalar mass. The degree of self-interaction is shown in the colour bar on its side (*left*). Same plot but the plotted points now also allow for a sizeable self-interaction. The relevant range of variation of f is shown in the colour palette (*right*).

where m_T denotes the mass of the target nucleus and $\mu = m_T M_{DM}(m_T + M_{DM})^{-1}$ denotes the reduced mass of the nucleus-DM. The interaction with a nucleus with atomic number A and charge Z, then, is given by,

$$\frac{d\sigma(v, E_R)}{dE_R} = \frac{m_T}{2\mu^2 v^2}\sigma_{\mathrm{SI}}^T F^2(2m_T E_R) \tag{6.3}$$

where $\sigma_{\mathrm{SI}}^T = \dfrac{4\mu^2}{\pi}[Zf_p + (A-Z)f_n]^2$ is the DM-nucleus cross-section at zero momentum transfer. Also, f_p and f_n denotes couplings with p (proton) and n (neutron) respectively. We have

$$f_N = m_N \left(\overset{u,d,s}{\underset{q}{\Sigma}} f_q^N \frac{\lambda_q}{m_q} + \frac{2}{27}\overset{c,b,t}{\underset{Q}{\Sigma}} f_G \frac{\lambda_Q}{m_Q} \right); N \in \{p, n\}. \tag{6.4}$$

In the above expression λ_q denotes the effective coupling of χ_- with the quark q in the limit of small momentum transfer, and is given by $f y_q \sin\theta_{\mathrm{mix}}\cos\theta_{\mathrm{mix}}\left(\dfrac{1}{M_{H_1}^2} - \dfrac{1}{M_{H_2}^2}\right)$, where y_q denotes the Yukawa coupling for quark q. f_q^N denotes the contribution of quark q to the mass m_N of nucleon N. While the light quarks contribute to the nucleon masses directly, the heavy quark contributions to f^N appears through the loop-induced interactions with gluons. These are given by,

$$f_q^N = \frac{1}{m_N}\langle N|m_q \bar{q}q|N\rangle, \ f_G = 1 - \overset{u,d,s}{\Sigma} f_q^N. \tag{6.5}$$

Note that, since H_1 and H_2 mediated t-channel processes contribute, the s quark content of the nucleon can be of significant importance. Following `micrOMEGAs4.3.5` [140], we have used $\sigma_{\pi N} = 34$ MeV and $\sigma_s = 42$ MeV to determine the quark contents of the nucleon. Further, $F(q)$ denotes the nuclear form factor corresponding to a momentum transfer q.

However, since we are interested in the presence of a very light H_1, as required for the Sommerfeld enhancement of the self-interaction cross-section, the mediator mass can be comparable to or even smaller than the typical momentum transfer of $\mathcal{O}(100)\,\mathrm{keV}$ (for $\sim \mathcal{O}(100)\,\mathrm{GeV}$ DM).

In such cases, use of σ_{SI}^T, as described above, overestimates the direct detection constraint on $f\sin\theta_{\mathrm{mix}}$. In order to account for the same, we have introduced a factor $\dfrac{M_{H_1}^4}{(q^2 + M_{H_1}^2)^2}$ to the right hand side of eq. (6.3) [141]. For $k_{\max} \ll M_{H_1}$, this additional term simply reduces to 1, while for $k \gtrsim M_{H_1}$ this ensures the correct momentum dependence of the DM-nucleus interaction cross-section. Note that depending on the detector threshold, the minimum momentum transfer $q_{\min}$ is different, while the maximum possible momentum transfer $q_{\max}$ is set by v_{esc}. Typically $q_{\min}$ falls well below $1\,\mathrm{MeV}$, and assuming H_1 thermalizes with the SM particles, $q_{\min} \gg M_{H_1}$ would contribute to the additional relativistic d.o.f during BBN and would be in tension with the relevant observations.

We have modified the publicly available code DDCalc [142] to incorporate the above. We have then used this code to compute a Poisson likelihood with the predicted number of events for a specific direct detection experiment with a particular DM benchmark, and compare that with the likelihood for background-only hypothesis to constrain the model parameters $f\sin\theta_{\mathrm{mix}}$. This is shown in figure 9 (left) along with the self-interaction cross-section in the colour bar. The range of f used in the scan is from 10^{-5} to 1. On the right hand side, we show the same plot but this time only the points with strong self-interaction is plotted. The suitable range of f corresponding to this is shown in the adjacent colour bar. The direct detection constraints becomes more and more rigid as we increase the dark matter mass, being most tightly constraining at $M_{DM} \sim 50\,\mathrm{GeV}$. Then the bound weakens gradually as we increase the mass. This fact is also reflected in the figure through the arrangement of the different exclusion lines. The line corresponding to the $50\,\mathrm{GeV}$ dark matter rules out the largest volume of the parameter space, whereas the $500\,\mathrm{GeV}$ dark matter corresponds to a looser constraint than $50\,\mathrm{GeV}$ (but tighter than $5\,\mathrm{GeV}$) as expected.

The improved calculation of direct detection constraints opens up a large part of the parameter space as opposed to the conventional calculation. A comparison between the two methods in shown in figure 10. In case of low mass DM ($2\,\mathrm{GeV} \lesssim M_{DM} \lesssim 4\,\mathrm{GeV}$), CDMSLite [143] puts the dominant constraint.[13] For $M_{DM} \gtrsim 5\,\mathrm{GeV}$ onwards Xenon-1T [139] puts forward the most stringent limits.[14]

Before moving forward, some important points are in order. Firstly, till now we were discussing about direct detection experiments which measures nuclear recoil when a dark matter particle hits them. Unfortunately, if dark matter mass goes down below ($\mathcal{O}(300)\,\mathrm{MeV}$) then nuclear recoils are not an effective method to detect dark matter since recoils energies become pretty low. The effective method is these low mass regions is to measure electron recoils. Experiments like SENSEI [145], XENON-10 [146], XENON-100 [147], SuperCDMS [148] and DarkSide-50 [149] have measured dark matter electron scattering

---

[13]For even lower masses, CRESST-III [144] has better sensitivity, however, we have not explored the region $M_{DM} \lesssim 1\,\mathrm{GeV}$.

[14]Note that Lux [31] and Panda-II [32] also lead to comparable constraint as Xenon-1T [139].
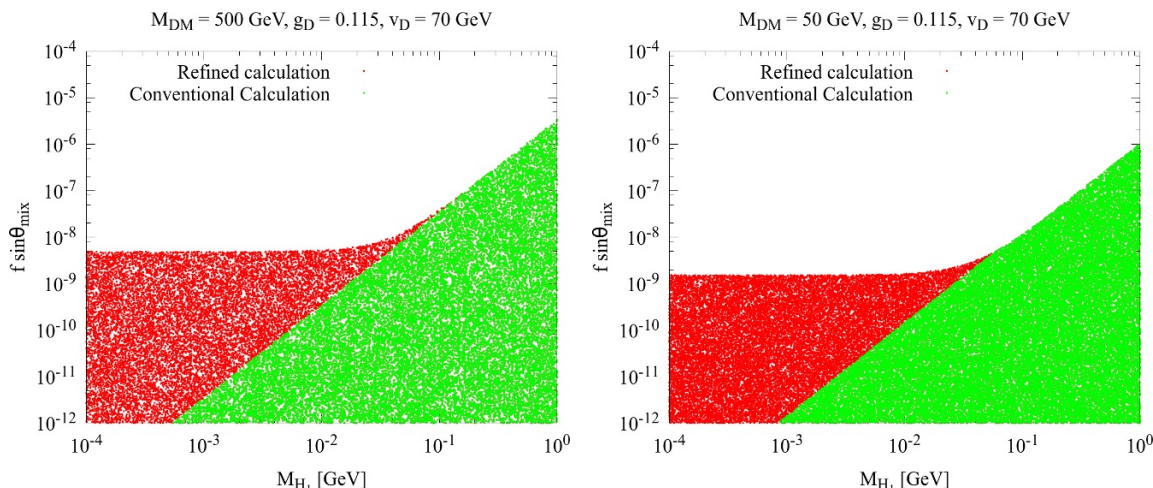
Figure 10. Comparison of calculation of constraints from direct detection experiment `Xenon-1T` [139] done using the conventional and refined calculation for a 500 GeV dark matter (*left*). Same plot but with a 50 GeV dark matter. Note the slight shift of the point where our refined calculation meets the conventional calculation in this plot when compared with the neighbouring plot. The shift is towards the left for a lighter dark matter as expected (*right*).

cross-sections and have put constraints on the latter. As mentioned in [150], the upper bound on dark matter electron cross-section on a $\mathcal{O}(100)$ MeV dark matter is $\sim 10^{-38}$ cm² (with form factor F_{DM} set to unity). The dark matter electron cross-section in our model goes as $\sim f^2 y_e^2 \sin^2 2\theta_{\text{mix}}$, where y_e is the electron Yukawa coupling and hence expected to be quite small. For the case of a light mediator (but $M_{H_1} > 10$ MeV to avoid BBN constraints), the dominant contribution to the dark matter electron cross-section comes from the t-channel process. For $M_{DM} \lesssim 1$ GeV but greater that M_{H_1} and M_e, the DM-electron cross-section at small center of mass momentum is approximately given by:

$$\sigma_e \simeq f^2 y_e^2 \sin^2 \theta_{\text{mix}} \Bigg(8 \ln \left(\frac{4M_{H_1}^2}{4M_{H_1}^2 + 9M_{DM}^2} \right) \left(M_{H_1}^2 M_{DM}^2 - 18M_{DM}^4 + 4M_{H_1}^4 \right)$$
$$+ 9 \left(8M_{H_1}^2 M_{DM}^2 - 7M_{DM}^4 \right) \Bigg) \Bigg/ \left(576 \, \pi \, M_{DM}^4 \left(4M_{H_1}^2 + 9M_{DM}^2 \right) \right) \tag{6.6}$$

For a 100 MeV dark matter, cross-section with electrons turn out to be roughly $\sim 5.6 \times 10^{-50}$ cm² for $f \sim \mathcal{O}(0.1)$ and $\sin \theta_{\text{mix}} \sim 10^{-5}$. These values of f and $\sin \theta_{\text{mix}}$ also gives rise to sizeable self-interaction as discussed earlier.

Secondly, DM direct detection experiments are not sensitive once the cross-section becomes comparable to the neutrino nucleon coherent scattering cross-section [151]. This imposes a lower limit on constraining $f \sin \theta_{\text{mix}}$. For example, with a 50 GeV dark matter and $\mathcal{O}(1)$ GeV H_1 mass, we found earlier that $f \sin \theta_{\text{mix}} \lesssim 10^{-6}$. With future direct detection probes, for this particular choice of parameters, this constraint can be further lowered by roughly one order of magnitude before it hits the neutrino floor. With lighter mediator mass, however, $f \sin \theta_{\text{mix}}$ can be lowered further (by a few orders) before it merges with the neutrino cross-section (see figure 10).

6.2 (Thermal) relic density of dark matter

From the discussions in the previous sections, we find that in order to satisfy constraints from direct detection experiments and allow sizeable self-interactions at the same time, the required value of $\sin\theta_{\mathrm{mix}}$ is actually very small ($\simeq 10^{-5} - 10^{-7}$, for a suitable f, where the latter is fixed from considerations of self-interactions). With such small values of mixing angle, the standard procedure for calculation of relic density (assuming prior thermalization and a subsequent freeze-out) is placed under scrutiny and demands some in-depth analysis before proceeding further. In this work, we have already assumed that the kinetic mixing between Z and Z_D is very small (denoted by ϵ_g). Hence, the scalar mixing angle (θ_{mix}) is the only possibility through which the dark sector can communicate with the SM sector and eventually can come to equilibrium with the photon bath. At high temperature, well above EWSB, the most important interaction leading to effective thermalization of the DM and the SM sectors is governed by the coupling λ_{mix} ($H_2H_2 \leftrightarrow H_1H_1$ type of interactions). Note that, $\sin\theta_{\mathrm{mix}}$ depends on *vevs* via eq. (2.10), and thus would be negligible well above EWSB.[15] The cross-section of $H_2H_2 \leftrightarrow H_1H_1$ is given by $\sigma \sim \frac{\lambda_{\mathrm{mix}}^2}{32\pi s}$, where we have neglected the thermal masses of the scalars and treated these as relativistic species. The two systems can thermalize if the rate of interaction can exceed that of the Hubble expansion at a (sufficiently) high temperature. The rate of annihilation is given by $\Gamma = n^{\mathrm{eq}}\langle\sigma v\rangle$, where n^{eq} is the equilibrium number density of the particle under consideration and v is the relative velocity of the annihilating particles. If at some temperatures $T \gg T_\gamma^{\mathrm{EWSB}}$ ($\simeq 160\,\mathrm{GeV}$) [153, 154], $\Gamma/H \sim 1$, then we can safely conclude that the dark and the visible sectors did thermalize in the early universe. Here H is the Hubble expansion rate and is given by $1.67\sqrt{g_\star}\frac{T^2}{M_{\mathrm{Pl}}}$, where $g_\star$ is the degree of freedom and M_{Pl} is the Planck mass. In our discussion, we have taken $T \sim 10^5\,\mathrm{GeV}$. We find, that for the two sectors to be in equilibrium at such temperatures $\lambda_{\mathrm{mix}} \gtrsim 10^{-5}$ (figure 11). Hence for values smaller than this, the two sectors will fail to thermalize and usual techniques of calculation of relic density by freeze-out mechanism will lead to incorrect results.

In the previous section, we derived constraints on $f\sin\theta_{\mathrm{mix}}$ from direct detection experiments and plotted points which were simultaneously allowed by it and also can lead to sizeable self-interactions. The range of f found from such considerations was $10^{-3} \lesssim f \lesssim 1$. This in turn constrains the scalar mixing angle (depending on the dark matter mass). But, we know,

$$\sin 2\theta_{\mathrm{mix}} = \frac{\lambda_{\mathrm{mix}}\,(M_{\mathrm{Z_D}}/g_D)\,v_h}{M_{H_2}^2 - M_{H_1}^2} \tag{6.7}$$

Hence, we can try to visualize the part of the parameter space (in $M_{Z_D} - \lambda_{\mathrm{mix}}$ plane, say) that can give rise to a thermal relic. Two values of f and two different dark matter masses were chosen for demonstration purpose. It is evident from figure 12, that with increasing f the allowed region decreases for a given dark matter mass. On the whole, light dark matters are more favoured with respect to the heavier ones in the thermal scenario. The value of the dark gauge coupling g_D was however arbitrarily fixed to 0.2 in these plots.

---

[15]However, close to EWSB, the temperature dependance of mixing angles and scalar masses need to be considered, see e.g. [152].
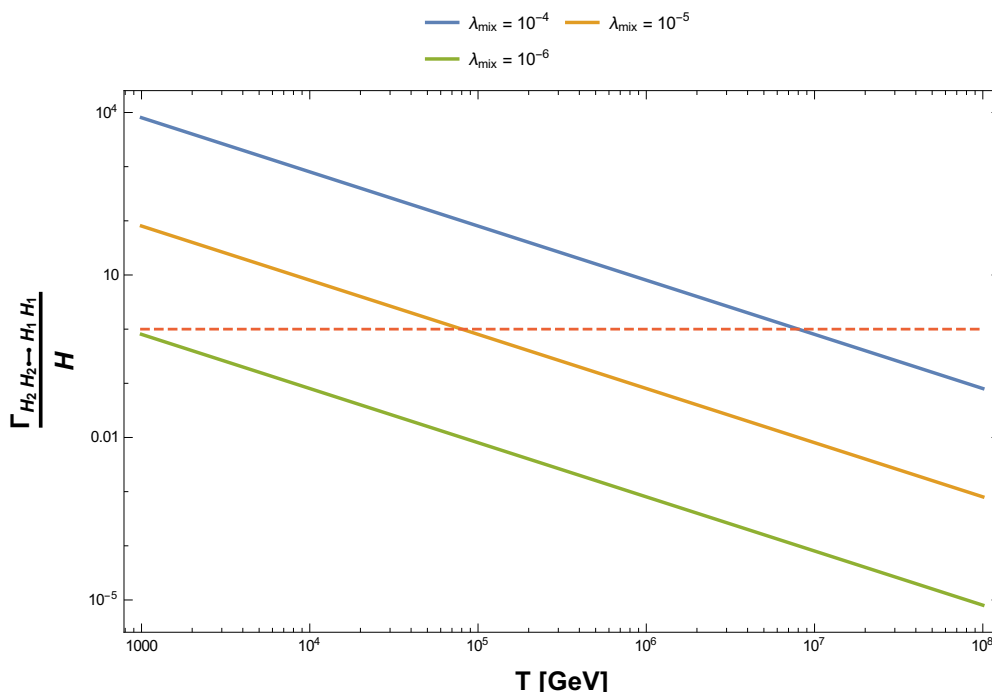
Figure 11. Comparison of the rate of $H_2 H_2 \leftrightarrow H_1 H_1$ vs the Hubble expansion rate in the early universe for different values of the quartic coupling λ_{mix}. The red dashed line signifies the temperature at which they were equal. The dark and the standard model sectors were in thermal contact before this epoch.

If we lower g_D, the allowed parameter space decreases as expected. In principle, g_D can be fixed from considerations of correct thermal relic. The constraint of $f \sin \theta_{\text{mix}}$ from direct detection is dependent on the value of the mass of the light scalar. For conservative estimates we have taken the minimum value of M_{H_1} allowed from BBN i.e. $\sim \mathcal{O}(10)\,\text{MeV}$. For higher values of the mediator mass more allowed regions are expected to open up.

Finally, analogous to the plot in the previous section, we show the range of variation of relic density alongside that of λ_{mix} for the points allowed by direct detection experiments and at the same time giving rise to sizeable self-interaction in figure 13. From this, we can easily conclude that light dark matter is our best bet if one wishes to stick to the (usual) regions of thermal relic density.

The dominant contributing channel to the thermal relic density can be broadly classified into three classes:

- $\chi_1 \chi_1 \leftrightarrow H_1 H_1$: the cross-section solely depends on f ($\sigma \sim f^4$). This type of channel can in general be present in simple extensions of SM (for example in cases where we have only a scalar portal mediating the dark sector and the visible sector). We have seen that the requirement of strong self-interaction among the dark matter particles pushes f towards higher values ($f \sim \mathcal{O}(0.1)$). So, this may lead to under abundance in usual circumstances. But in our model since the dark matter χ_- is a Majorana particle, this type of annihilations are p-wave suppressed, consequently
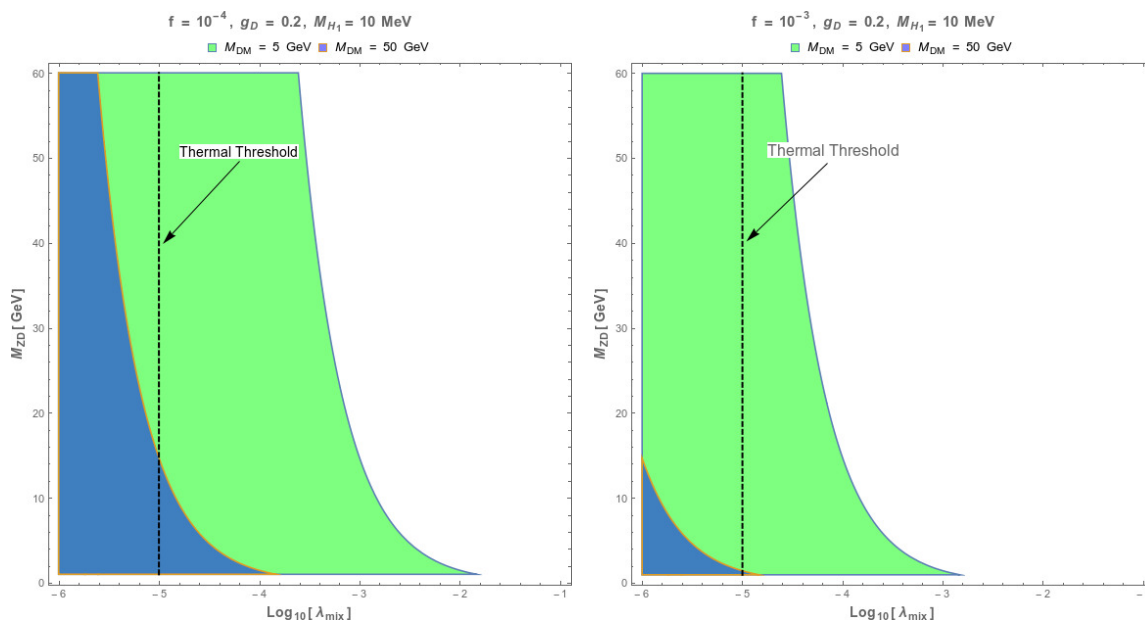
Figure 12. Plots showing the allowed region for accommodating a thermal dark matter in $M_{Z_D} - \lambda_{\mathrm{mix}}$ plane. The region on the right from the black dashed line is the region that can support thermal dark matter ($\lambda_{\mathrm{mix}} \gtrsim 10^{-5}$).
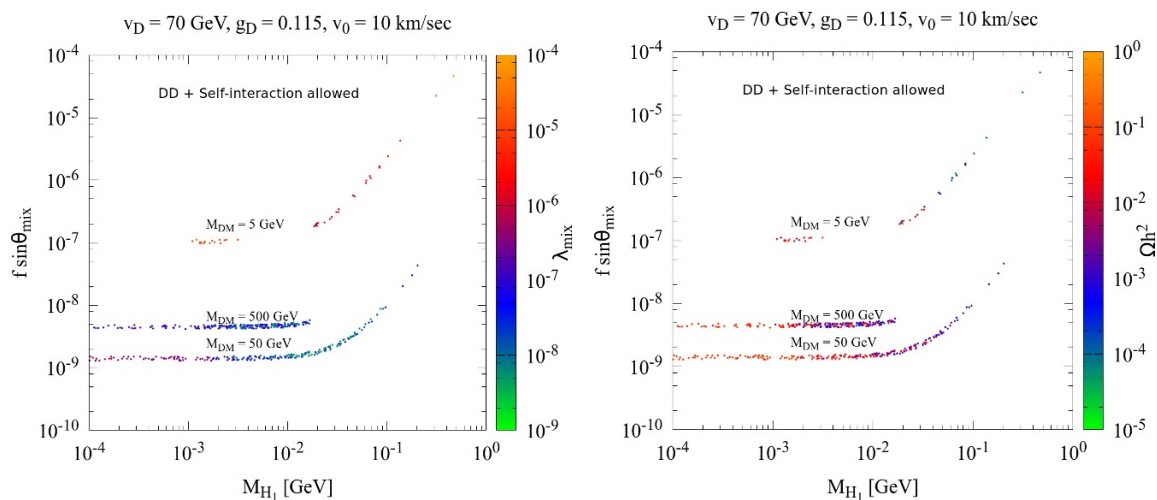
Figure 13. Plots showing the variation of relic density along with the quartic coupling, λ_{mix} in the colour bar for points allowed by direct detection constraints and also having sizeable self-interactions.

Thermal Benchmark										
M_{DM}	M_+	M_{Z_D}	M_{H_1}	λ_ϕ	λ_{mix}	g_D	$\sin\theta_{\mathrm{mix}}$	f	Ωh^2	$\frac{\sigma_{\mathrm{self}}}{M_{\mathrm{DM}}}$
2 GeV	5.7 GeV	2.4 GeV	20 MeV	2.2×10^{-7}	4.5×10^{-5}	0.08	2.04×10^{-5}	0.09	0.12	0.11 barn GeV^{-1}

Table 2. Table demonstrating a benchmark where the thermal relic scenario can be realised. It satisfies all the constraints as well has sizeable self-interactions at virialized velocities of $v_0 \sim \mathcal{O}(10)$ km sec^{-1}. The dominant channel contributing to the thermal relic density is $\chi_1\chi_1 \leftrightarrow H_1H_1$. Since the dark matter mass is beyond the reach of Xenon-1T [139], this specific benchmark is checked against experiments which are sensitive to light dark matters i.e. CRESST-II [155] and CDMSlite (run-2) [156].

satisfying thermal relic density (see, for example, table 2). In such cases, for points with correct relic density, we have $f \sim \sqrt{M_{\mathrm{DM}}(\text{in TeV})/1\,\text{TeV}}$ (assuming only t and u channels are the dominant ones, which is the case here because of small values of λ_ϕ). However, for general dark matter masses, correct relic density and large self-interactions cannot always be satisfied by adjusting this single parameter f, and may lead to over abundance.

- $\chi_1\chi_1 \leftrightarrow Z_D Z_D$: if it is over abundant, in order to obtain the correct relic abundance, we in principle can resort to a new channel employing the extra dark gauge boson Z_D. This type of channels are also a generic feature of minimal extensions of SM by a new local gauge group. The cross-section is now governed by both f and g_D ($\sigma \sim f^2 g_D^2$ or g_D^4, depending on which channel has the dominant contribution). The dark gauge coupling can be tuned to adjust the present day relic density to the observed value. Since g_D does not contribute to the self-interaction of dark matter, this parameter can be freely chosen to fix the relic, while f is fixed to a value that gives strong self-interaction between the dark matter particles. The mass of the dark matter particle is also constrained now such that $M_{DM} > M_{Z_D}$.

  In our case, from figure 2, we however find that for $M_{\mathrm{DM}} \gtrsim 10\,\text{GeV}$ and $M_{H_1} \gtrsim 10\,\text{MeV}$, those points with sizeable self-interactions (and consequently with $f \sim \mathcal{O}(0.1)$), the $\chi_1\chi_1 \leftrightarrow H_1H_1$ cross-section is itself too large rendering the dark matter under abundant. Thus, having this extra channel depending on g_D will not be helpful in practice to fix the relic density.

- $\chi_1\chi_2 \leftrightarrow A\,B$ (co-annihilation): thermal relic density in principle can also be dominated by co-annihilation cross-sections of χ_1 (DM) and χ_2 annihilating to A and B. The impact of co-annihilation is determined by the mass difference of the two dark states. It is strongest if the mass splitting is small. The mass splitting is given by $\Delta m_\chi = \sqrt{2} f\, v_D$. On the other hand, self-interaction demands for large values of the Yukawa coupling f. Thus co-annihilation fails to be the dominant contributor to the relic density of dark matter in our case.

To summarize, thermal dark matters which are strongly self-interacting and also respect constraints from direct detection experiments, as well as have observable collider signatures, should be light, i.e., $\lesssim \mathcal{O}(5)\,\mathrm{GeV}$. To get a better feel of the numbers let us consider a dark matter of order $\mathcal{O}(500)\,\mathrm{GeV}$. From figure 9 we find that $f\sin\theta_\mathrm{mix} \lesssim 6\times10^{-9}$ for $M_{H_1} \sim \mathcal{O}(10)\,\mathrm{MeV}$. The mediator should be light to allow for large self-interaction cross-section but not too light so as to violate bounds from BBN ($\gtrsim \mathcal{O}(10)\,\mathrm{MeV}$). Also, for sizeable self-interaction at these dark matter and mediator masses, we found that $f \sim \mathcal{O}(0.1)$. Taking v_D to be as low as $\sim \mathcal{O}(1)\,\mathrm{GeV}$, we find $\lambda_\mathrm{mix} \lesssim 7.7\times10^{-6}$ and that falls below our derived limit of thermal threshold. Hence, for high mass dark matter, we are almost out of points in the parameter space that satisfies all of our aforementioned desired criteria. Light dark matters are hence more favourable in our scenario. Even for a $\mathcal{O}(5)\,\mathrm{GeV}$ dark matter, direct detection experiments force $f\,v_D \lesssim 0.25$. For reasons previously mentioned, with $f \sim 0.1$ we find $v_D \lesssim 2.5$. Along with this, requirement of $\lambda_\mathrm{mix} \gtrsim 10^{-5}$ (thermalizability) and not too small Z_D mass restricts our allowed parameter space quite heavily.

Next, as a concrete example, we present a specific benchmark in table 2 which illustrates that for specific choice of parameter values one can indeed have a perfectly thermal scenario satisfying all the constraints and also having a sizeable self-interactions although only with small dark matter masses.[16] In the next section we will discuss about the future detection prospects of our scenario in colliders.

7 Future searches

From the discussions in the perspective of dark matter phenomenology, we have thus been able to convince ourselves that for a thermal dark matter with large self-interactions we need very light H_1 as the mediator ($\sim \mathcal{O}(1)$) GeV. In the following sections we will investigate about the future of prospects and detectability of our model from a collider perspective. We probe the prospect of future collider experiments and estimate their effect on the parameter space which survives the current constraints as discussed in section 5.

7.1 Future prospects at ILC

Uncertainties in Higgs boson couplings to various SM final states from a combination of global fit of Higgs coupling measurements at the ILC have been presented in [157]. Combination of the results of Higgs coupling measurements from the $300\,\mathrm{fb}^{-1}$ run of LHC, and 500 GeV run of ILC, may lead to an error of 0.3% in HZZ coupling [157]. Correspondingly, we test the impact of this constraint on our parameter space by choosing those points which generate $\mu_{ZZ^*}^{ggF}$ in the range of $0.997-1.003$. Such parameter space points have been shown in orange color in figure 14. The blue colored points in figure 14 correspond to the entire set of parameter space scanned by us. It can be observed that the projected reach of ILC is $\sin\theta_\mathrm{mix} \gtrsim 7\cdot10^{-3}$ which is roughly 1 order of magnitude stronger than the current LEP results.

---

[16]This benchmark is compliant with constraints from BBN since the mass of the mediator $M_{H_1} \gg 1\,\mathrm{MeV}$ consequently rendering it to be non relativistic during the time of BBN. Furthermore, the lifetime of H_1 is also less than 1 sec (i.e. onset of BBN).
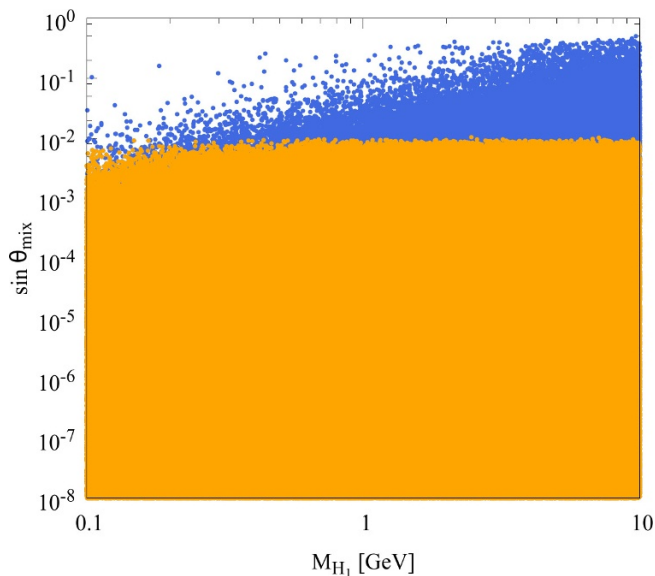
Figure 14. Parameter space points in the $M_{H_1} - \sin\theta_{\text{mix}}$ plane. The blue colored points are excluded by the projected sensitivity of ILC+LHC to probe HZZ^* coupling within 0.3%.

7.2 Exclusions from future SHiP and LZ experiments

Continuing our discussion of section 5.4, we show the projected reach of two relevant future experiments, namely, SHiP [158] and LZ, in figure 15. The projected sensitivity of SHiP is remarkably strong when compared to the current experiments. For $M_{H_1} \sim 1\,\text{GeV}$, the current limits exclude $\sin\theta_{\text{mix}}$ above $\sim 10^{-3}$, whereas, SHiP is projected to probe until $\sin\theta_{\text{mix}} \sim 10^{-5}$. LZ is expected to gain effectiveness in the $O(GeV)$ region, and is expected to improve upon the existing sensitivity by around an order of magnitude.

As seen from the findings of the preceding three subsections, a hunt for a light scalar mediator in future colliders seem to be challenging. Our model however also possesses an $\mathcal{O}(1)\,\text{GeV}$ Z_D and dark matter. Hence, we can instead try searching for this dark photon in future colliders. It is important to note that the analysis performed in the next two subsections would comply only in the case of a promptly decaying Z_D boson. The total decay width of Z_D is proportional to ϵ_g^2. A value of $\epsilon_g^2 \gtrsim 10^{-12}$ results in a lifetime which is compatible with the regime of prompt decay. Smaller values of ϵ_g ($\lesssim 10^{-6}$) results in decay lengths of the order of $\sim 10^{-5}$ m or higher, resulting in a late decaying phenomena. The generic collider features of a late decaying Z_D has been discussed in section 7.3.4.

7.3 Future prospects at HL-LHC

We begin this subsection by a discussion of the future prospects of the light scalar mediator (H_1). We also perform a search for Z_D in the $H_2 \to Z_D Z_D \to 4\mu$ channel and derive upper limits on $\sigma_{ggH_2}/\sigma_{ggH_{\text{SM}}} \times Br(H_2 \to Z_D Z_D)$ for the case of HL-LHC. We also present a search strategy to probe Z_D in the $4\mu + \not{E}_{\text{T}}$ final state, produced via cascade decay of $\chi_+\chi_+$ pair produced from a H_2. Finally, we conclude this subsection by a discussion of the prospects of a late decaying Z_D at the HL-LHC and HE-LHC.
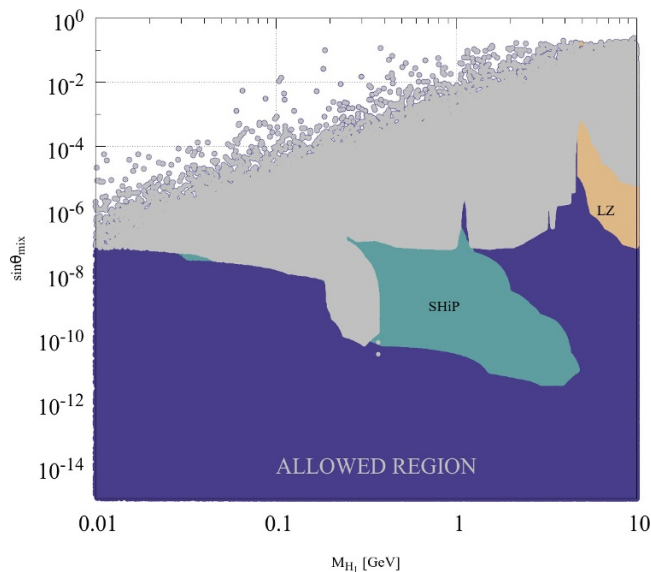
Figure 15. Parameter space points in the $M_{H_1} - \sin\theta_{\mathrm{mix}}$ plane. The grey colored points are excluded by the current search limits from beam dump experiments and flavor physics experiments (figure 8). The green colored points will be within the projected reach of SHiP experiment while the brown colored points could be probed by the proposed LZ.

7.3.1 $H_2 \to H_1 H_1$

We have already discussed in section 5.3 that ATLAS and CMS have performed different searches for the Higgs boson decaying into two spin-zero particles in various final state using Run-I and Run-II datasets: 4τ [101], $2\mu 2b$ [96, 101], $2\mu 2\tau$ [100–102], 4μ [95, 98, 104], 4τ [105, 106], $2\tau 2b$ [99, 107], $4b$ [97]. Apart from these analyses, CMS has also looked for direct production of a light pseudoscalar Higgs boson in the dimuon decay channel using LHC 7 TeV data [159] and the limits are not very strong yet. For lower values of M_A or M_{H_1} (in the range 1 to 8 GeV) much stronger bounds have been obtained by ATLAS in 4μ channel [95] (shown as black dashed line in figure 6). Rest of the channels like $2\mu 2b$ [96, 101], $2\mu 2\tau$ [100–102], $2\tau 2b$ [99, 107], etc. are sensitive for higher mass range (typically 15 GeV $< M_A < 62.5$ GeV).

The possibility to probe a light pseudoscalar particle from Higgs decays at the 14 TeV LHC has been studied in [160] for $2\mu 2\tau$ final state. This search covered the mass range: $2M_\tau < M_A < 2M_b$. Using the upper limit obtained from this analysis, expected future reach for 14 TeV LHC with integrated luminosity $\mathcal{L} = 300\ fb^{-1}$ have been translated in [161] (see figure 7 of [161]). The projected upper limit on the branching ratio of $H_2 \to H_1 H_1$ is roughly 5% [161], and has been represented in figure 16 as a dashed red line.[17] The color code of figure 6 has been followed in figure 16.

For our case we find that $H_2 \to H_1 H_1$ branching ratios lie in the range 10^{-3} to 10^{-6}, which will be beyond the reach of HL-LHC in $2\mu 2\tau$ final state.

---

[17]Under the assumption: $\sigma_{H_2}/\sigma_{H_{\mathrm{SM}}} = 1$.
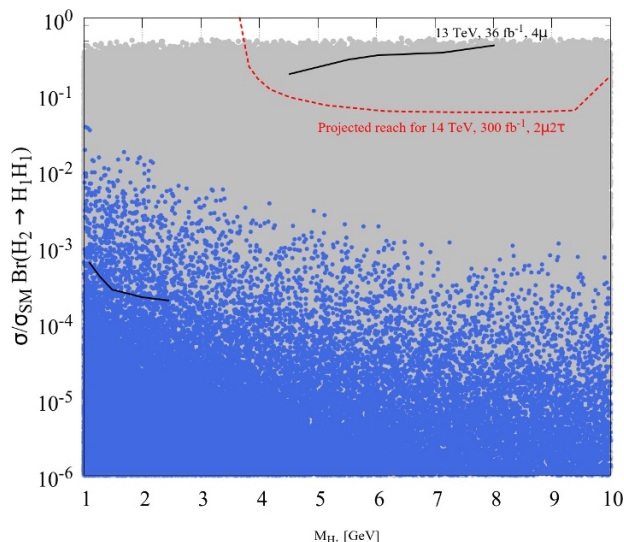
Figure 16. Scatter plot showing $\sigma_{H_2}/\sigma_{H_{\mathrm{SM}}} \times Br(H_2 \to H_1 H_1)$ vs M_{H_1}. The solid black line represents the upper limit on $\sigma_{H_2}/\sigma_{H_{\mathrm{SM}}} \times Br(H_2 \to AA)$ derived by ATLAS from search in the 4μ final state, using the LHC Run-II dataset corresponding to $\sim 36.1 \ fb^{-1}$ [95]. The dashed red line corresponds to the future projection for 14 TeV, 300 fb^{-1} LHC derived in [161] using the results from [160], assuming $\sigma_{H_2}/\sigma_{H_{\mathrm{SM}}} = 1$.

In [162], the expected future reach at the 14 TeV LHC has been studied for $H_2 \to AA \to 4b$ and $H_2 \to AA \to 2b2\tau$ final states, where the Higgs boson is produced in association with a W or Z boson. This analysis is sensitive for $M_A > 10 \,\mathrm{GeV}$ and $4b$ final state is more promising than the $2b2\tau$ channel. The potential of an exotic Higgs decay search for $H_2 \to XX \to 2b2\mu$ $(X = H_1/A)$ in the mass range of 15 to 60 GeV has been presented in [163]. It is found that $Br(H_2 \to 2X \to 2b2\mu)$ can be constrained at the few $\times 10^{-5}$ level at the HL-LHC. Both these analyses [162, 163] are not sensitive for the parameter space of our interest $(M_{H_2} < 10 \,\mathrm{GeV})$.

7.3.2 $H_2 \to Z_D Z_D \to 4\mu$

A detailed search analysis for Z_D is presented $(M_{Z_D} = 2 - 12 \,\mathrm{GeV})$, using the process $pp \to H_2 \to Z_D Z_D \to 4\mu$ final state, in the context of 14 TeV run of LHC at an integrated luminosity of 3000 fb^{-1}. This mass range of Z_D is particularly motivated by the preferred choice of a small v_D which is favourable for thermalization (as discussed in section 6.2), which eventually results in a small Z_D mass. Below $M_{Z_D} \lesssim 2 \,\mathrm{GeV}$, prospects of observability in collider searches becomes very weak. At the LHC, the Higgs boson is dominantly produced via the gluon fusion mode (ggF). The ggF mode overshadows the other modes of Higgs production, such as vector boson fusion (VBF), associated production with b quarks $(b\bar{b}H_2)$ and associated production with top quarks $(t\bar{t}H_2)$, and therefore, in the current analysis, we consider only the ggF mode of Higgs production.

The signal sample involves the process: $gg \to H_2 \to Z_D Z_D \to 4\mu$. Dominant backgrounds arise from electroweak $4l$ production and the $H_2 \to ZZ^*$ decay process. The $gg \to H_2$ samples have been generated using MadGraph5 [164], with M_{H_2} fixed at 125 GeV.
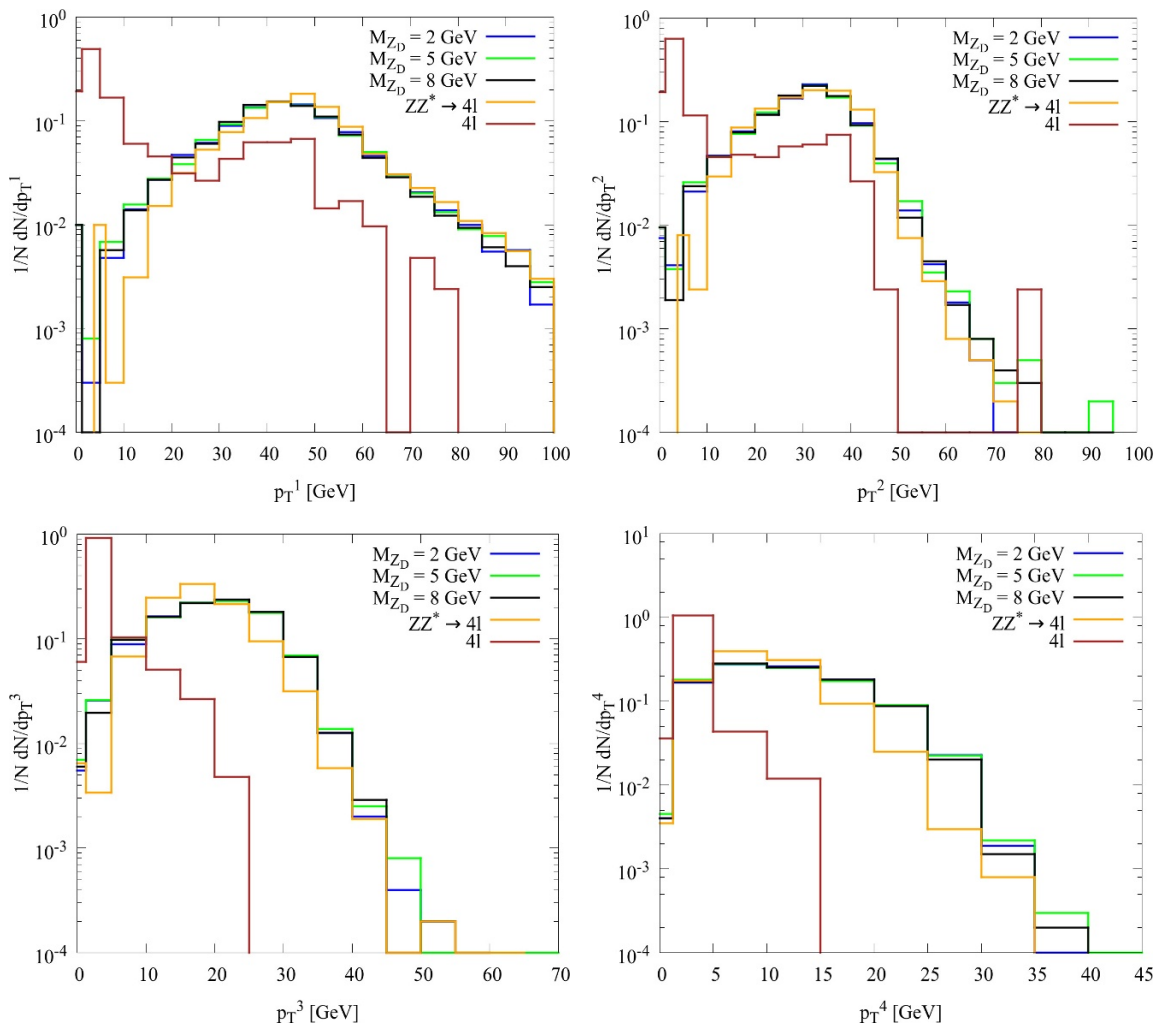
Figure 17. Transverse momentum (p_T) distribution of the final state muons at the partonic level. The blue, green and black colored lines correspond to the signal event generated with different Z_D masses, $M_{Z_D} = 2$, 5 and 8 GeV, respectively. The orange and the brown colored line represents the p_T distribution of the $ZZ^* \to 4l$ and electroweak $4l$ background.

The subsequent decay process, followed by showering and hadronization is performed by Pythia-6 [165]. The $4l$ background has been generated by MadGraph5 at the partonic level, while Pythia-6 has been used for showering.

The final state muons are required to have transverse momentum, $p_T > 2.6$ GeV and must lie within a pseudorapidity range of $|\eta| < 4.0$. Isolation condition requires the sum of transverse momentum of other tracks, excluding the leading four muons, within a cone of radius $\Delta R = 0.2$ around the muon to be less than 30% of the p_T of the muon. Furthermore, if the ΔR between the muon and the reconstructed jet is less than 0.4, then the muon is removed. Event selection requires exactly 4 muons to be present in the final state. Before moving on to discuss the choice of selection cuts, we discuss the kinematic distribution of the four muons in the final state. In this context, we choose three different
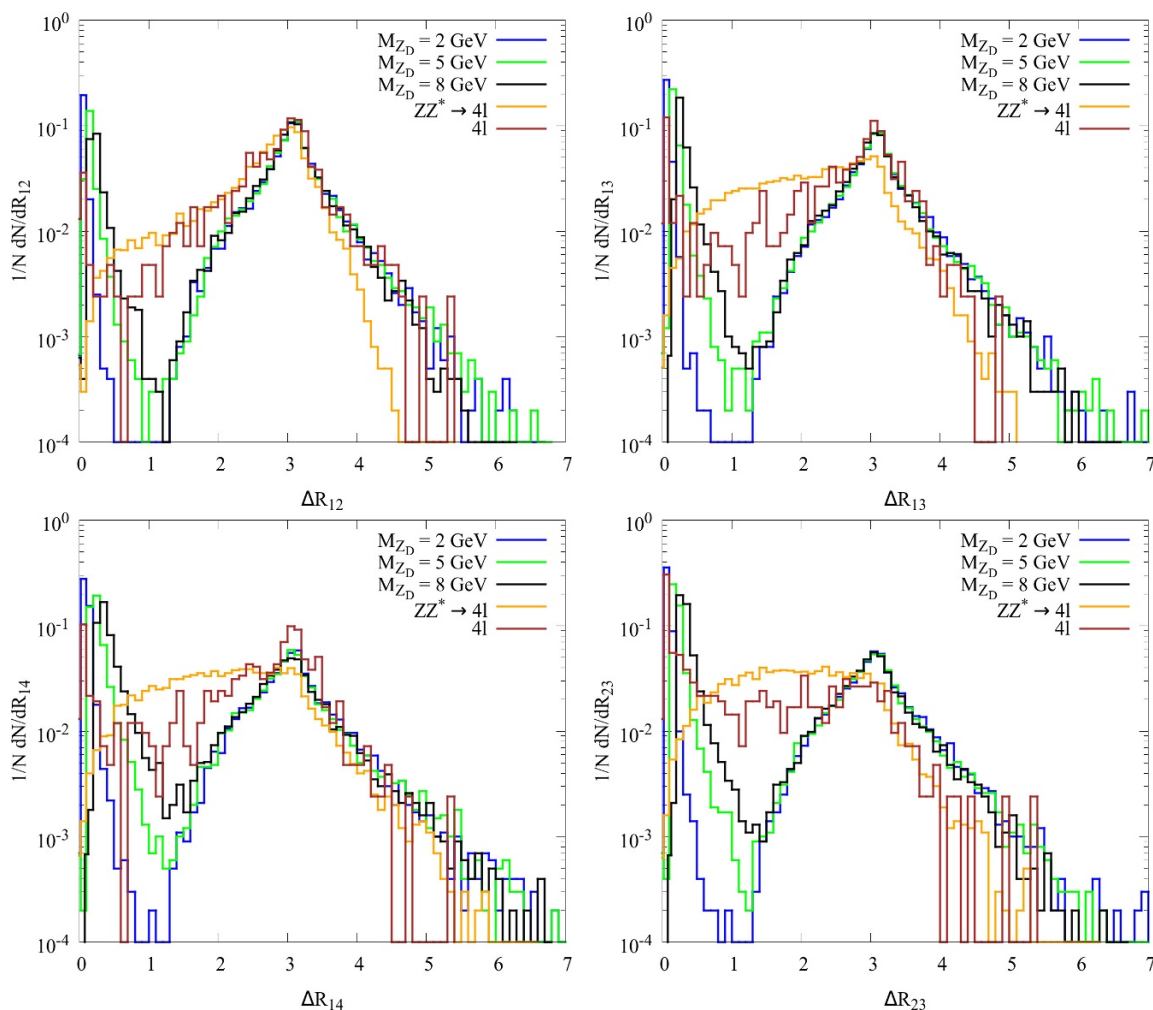
Figure 18. Normalised distribution showing ΔR between various final state muon pairs. The color codes are the same as that of figure 17.

values of $M_{Z_D} = 2, 5, 8$ GeV to generate the signal. The p_T distribution of the four muons from the background and the benchmark signals are shown in figure 17, where, the $4l$ and $H_2 \to ZZ^*$ backgrounds have been described by brown and orange colored lines, respectively. We would like to mention that the muons have been p_T ordered, and therefore, p_T^1 corresponds to the highest p_T muon while p_T^4 represents the lowest p_T muon. The blue, green and black colored lines correspond to the p_T distribution of the signal samples with $M_{Z_D} = 2, 5, 8$ GeV, respectively.

The signal samples and the $H_2 \to ZZ^*$ background yields a similar p_T distribution, while the $4l$ background peaks at very low values of p_T. Taking motivation from a similar search analysis by the ATLAS collaboration [95], and the p_T distribution of the $4l$ background, we demand the highest p_T muon to have $p_T > 20$ GeV. The second and third leading p_T muons are required to have $p_T^2 > 15$ GeV and $p_T^3 > 10$ GeV, respectively. The angular distributions of the final state muons also provide an additional control to filter out the signal events. In this context, we show the ΔR distribution between all some of the

Selection cuts
(a). Exactly 4 muons in final state.
(b). $p_T^{\mu_1} > 20$ GeV, $p_T^{\mu_2} > 15$ GeV
$p_T^{\mu_3} > 10$ GeV, $p_T^{\mu_4} > 2.6$ GeV
$\lvert \eta \rvert < 4$
(c). $\Delta(R)(\mu_1\mu_3, \mu_1\mu_4, \mu_2\mu_3, \mu_2\mu_4) > 2$
(d). 0.88 GeV $< M_{12}^{inv}, M_{34}^{inv} < 20$ GeV
(e). Event veto if: $(M_{J/\Psi} - 0.25$ GeV$) < M_{12,34} < (M_{\Psi(2s)} + 0.30$ GeV$)$
$(M_{\Upsilon} - 0.70$ GeV$) < M_{12,34} < (M_{\Upsilon(3s)} + 0.75$ GeV$)$
(f). $M_{34}^{inv}/M_{12}^{inv} > 0.85$
(g). 120 GeV $< M_{4\mu}^{inv} < 130$ GeV

**Table 3**. Selection cuts for the cut-based analysis in the 4μ final state, following [95].

possible final state muon pairs in figure 18. Before specifying the selection cuts on the ΔR variables, it is important to discuss the criteria for formation of same flavor opposite sign (SFOS) muon pairs. The four muons in the final state are required to form two SFOS pairs. Each quadruplet of muon per event can result in two separate combinations of di-SFOS pairs. The di-SFOS pair which results in smaller difference of SFOS muon invariant masses is chosen to be the correct di-SFOS pair. The SFOS pair with invariant mass closest to the Z boson mass is referred to as the leading SFOS pair and its invariant mass will be represented by M_{12}, while M_{34} represents the invariant mass of the sub-leading SFOS pair. Henceforth, in this subsection, we will refer to the muons in the leading SFOS pairs as μ_1 and μ_2, while muons in the other SFOS pair will be referred to as μ_3 and μ_4. Now, we go back to the discussions on the ΔR distributions shown in figure 18. It can be observed that the backgrounds mostly peak around $\Delta R \sim 1 - 2.5$ region, while the signal events peak at two distinct regions, $\Delta R \sim 0$ and $\Delta R \sim 3$. The peak in the $\Delta R \sim 0$ arise from muon pairs which originate from the same Z_D pair, and therefore, mostly correspond to the same SFOS pair, while the $\Delta R \sim 3$ peak manifests from the muons belonging to different SFOS pairs. Deriving motivation from this observation, we impose a lower cut on ΔR between muon pairs from separate SFOS pairs, ΔR_{13}, ΔR_{14}, ΔR_{23}, $\Delta R_{24} > 2$.

In addition, the invariant mass of the SFOS pairs, M_{12} and M_{34} are required to lie within the range $0.88-20$ GeV, and the ratio M_{34}/M_{12} is required to be greater than ~ 0.85, following [95]. The invariant mass of the four isolated muons ($M_{4\mu}$) is also required to lie within $M_{4\mu} = 120 - 130$ GeV. We would like to mention that events with any of the SFOS pairs having invariant mass in the range of J/Ψ resonance ($M_{OS} = 2.846 - 3.9861$ GeV) or Υ resonance ($M_{\Upsilon(2s,3s,4s)} = 8.7603 - 11.1052$ GeV), are vetoed. The selection cuts are summarized in table. 3. The $t\bar{t}$ and $b\bar{b}ll$ backgrounds were also evaluated, and no events survived the selection cuts.

	Fraction of events surviving selection cuts from table. 3						U.L. [fb]	
	(a)	(b)	(c)	$(d)+(e)$	(f)	(g)	$\sigma_{H_2\to Z_D Z_D}$	
M_{Z_D} [GeV]	Signal						5σ	2σ
2	0.838	0.752	0.665	0.664	0.651	0.637	0.197	0.078
2.80	0.831	0.747	0.674	0.674	0.659	0.643	0.166	0.066
4	0.829	0.746	0.662	0.528	0.522	0.522	0.426	0.170
6	0.821	0.737	0.651	0.648	0.636	0.614	0.465	0.186
8.75	0.814	0.734	0.640	0.640	0.620	0.598	0.489	0.196
11.11	0.815	0.731	0.637	0.406	0.397	0.396	0.738	0.295
12	0.812	0.729	0.621	0.580	0.573	0.568	0.515	0.206
	Background yield (14 TeV 3000 fb^{-1})						Cross-section before cut (a)	
$4l$	$2\cdot10^5$	$1\cdot10^5$	$1\cdot10^4$	773	169	6.87	458 fb	
$H_2\to ZZ^*$	2836	2583	588	42.9	13.4	11.8	1.0 pb	
$bbll$	$2\cdot10^5$	$4\cdot10^4$	$7\cdot10^3$	0	0	0	249.6 pb	

Table 4. The cut flow table showing the signal efficiency on successive application of selection cuts specified in table. 3, for M_{Z_D} = 2, 2.8, 4, 6, 8.75, 11.11, 12 GeV. The background yields corresponding to 14 TeV 3000 fb^{-1} LHC are also shown. The expected upper limits at 2σ level and the discovery reach at 5σ level, on $\sigma(gg \to H_2 \to Z_D Z_D)$, are also presented.

We perform the search for Z_D for different values of M_{Z_D} = 2, 2.85, 4, 6, 8.75, 11.11, 12 GeV, in the context of 14 TeV LHC corresponding to an integrated luminosity of 3000 fb^{-1}. The cut-flow table showing the signal and background yields are shown in table. 4. Upper limits are obtained on the ratio of production cross-section of SM-like H_2 through ggF mode (σ_{ggH_2}) and the ggF production cross-sections in SM ($\sigma_{ggH_{\mathrm{SM}}}$) times the branching fraction $H_2 \to Z_D Z_D$ at 5σ and 2σ, assuming zero systematic uncertainty, for the case of 14 TeV LHC operating an at integrated luminosity of 3000 fb^{-1}, as shown in figure 19. The branching ratio for $Z_D \to \mu^+\mu^-$ has been taken from [92]. ATLAS has also performed a search for Z_D in the $H_2 \to Z_D Z_D \to 4\mu$ final state using the LHC Run-II data collected at an integrated luminosity of $\sim$ 36.1 fb^{-1} [95], and has derived upper bounds on $\sigma_{ggH_2}/\sigma_{ggH_{\mathrm{SM}}} \times Br(H_2 \to Z_D Z_D)$ at 95% CL. We have represented these upper bounds as dashed red lines in figure 19. It can be observed that the upper limits
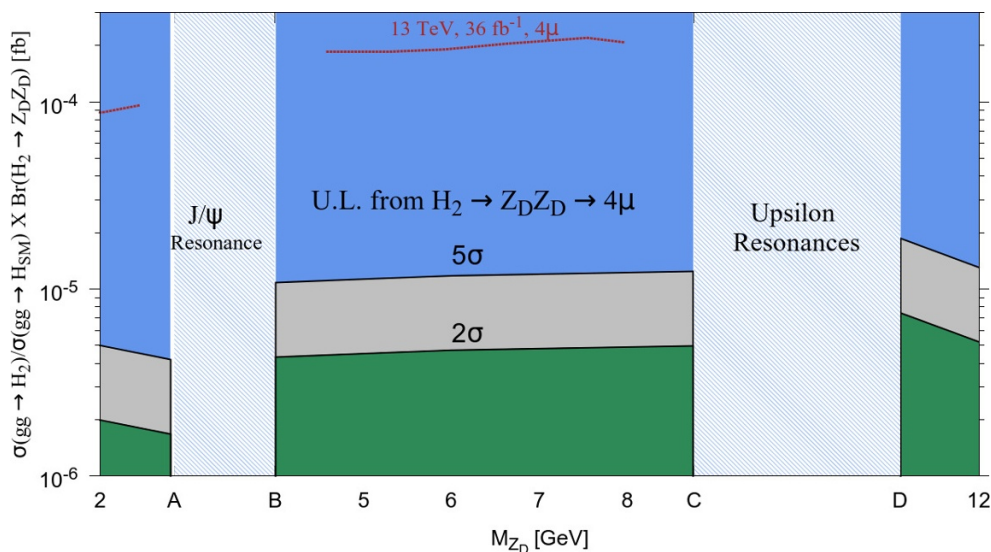
Figure 19. Upper limits on $\sigma_{ggH_2}/\sigma_{ggH_{\rm SM}} \times Br(H_2 \to Z_D Z_D)$ derived from Z_D search in the 4μ final state for 14 TeV LHC corresponding to an integrated luminosity of $3000\,{\rm fb}^{-1}$. The red dashed line corresponds to the upper limits on the same quantity, derived by ATLAS using LHC Run-II dataset collected at $\sim 36.1\ fb^{-1}$ [95].

for HL-LHC presented in figure 19 are roughly $\sim 10-15$ times stronger than the current bounds. These projected limits for HL-LHC would be capable to probe $\sin\theta_{\rm mix}$ up to $\sin 0.002\ (0.007)$ in the $M_{Z_D} \sim 2$ GeV ($M_{Z_D} \gtrsim 4$ GeV) region.

We conclude this subsection by evaluating the prospect of exclusion/discovery of the allowed benchmark point (BP1) of table. 2 by HL-LHC using the search limits derived in this subsection. BP1 furnishes a value of $Br(H_2 \to Z_D Z_D) \sim 5 \cdot 10^{-6}$ for $M_{Z_D} \sim$ 2.4 GeV, while $\sigma(gg \to H_2)$ attains a value of $\cos^2\theta_{\rm mix} \cdot \sigma(gg \to H_2)_{\rm SM}$, where, $\sigma(gg \to H_2)_{\rm SM}$ corresponds to the SM value of H_2 production cross-section in the ggF mode. At NNLO+NNLL level, $\sigma(gg \to H_2)_{\rm SM} = 39.56^{+7.32\%}_{-8.38\%}$ fb [166–168] for the 14 TeV run of LHC. Thus, $\sigma(gg \to H_2 \to Z_D Z_D)$ attains a value of ~ 0.2 for $\sqrt{s} = 14$ TeV. A comparison with the corresponding upper limit derived in figure 19 reveal that BP1 could be marginally probed at HL-LHC.[18] These searches have the potential to yield strong exclusion limits in the context of future high energy/ high luminosity colliders. Directly produced Z_D process, $pp \to Z_D \to \mu\mu$, could be another viable mode of probing Z_D. However, the signal is marred by a huge continuum Drell-Yan background. Consequently, the search strategies would involve an efficient treatment of low p_T muons. Some recent studies have focused on the case of such low p_T muons through scouting techniques [169, 170]. A more precise understanding of the background and derivation of further improved scouting techniques might help in alleviating $pp \to Z_D \to \mu\mu$ as an important probe of Z_D in the future runs of LHC.

[18]The reach can be further improved upon inclusion of $4e$ and $2e2\mu$ channels.
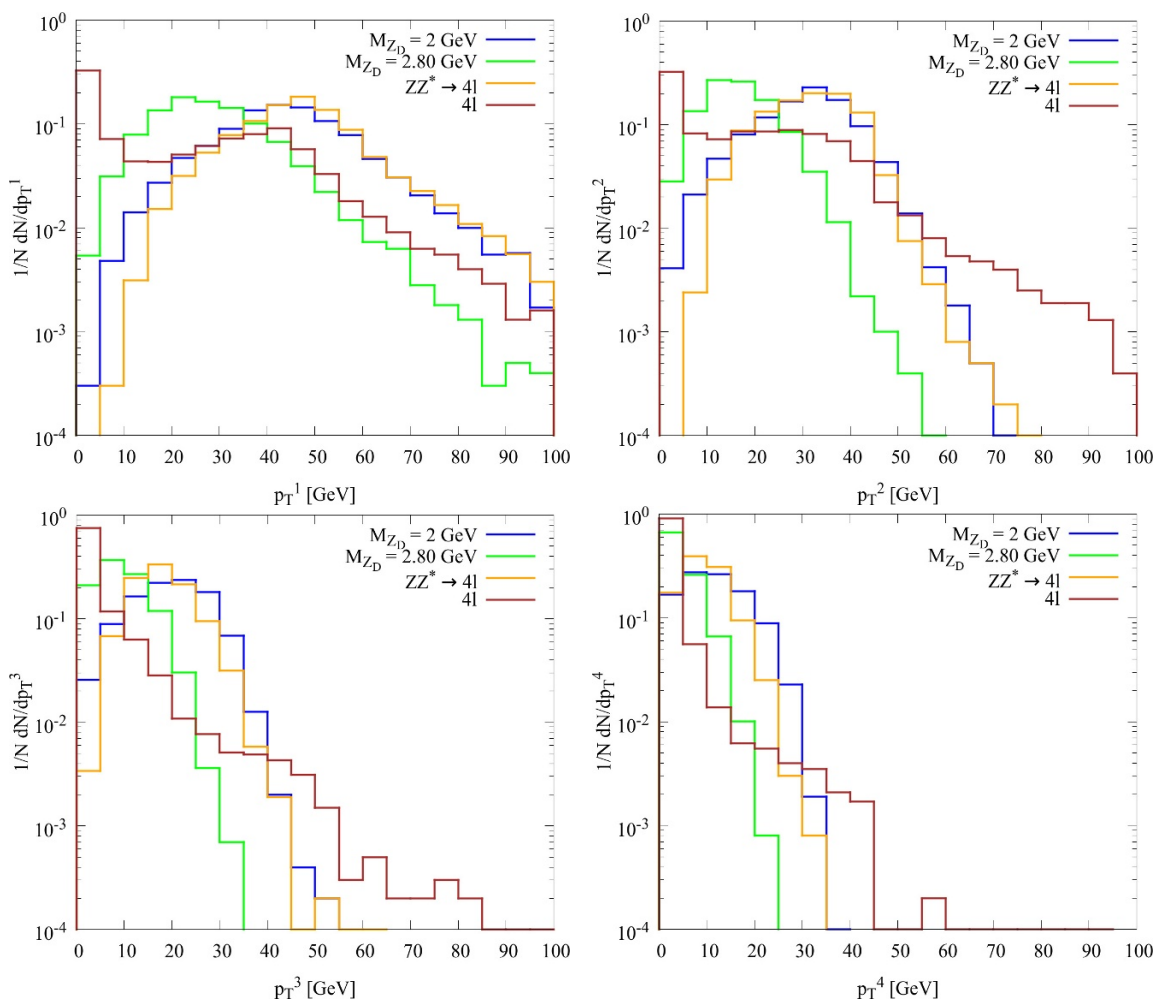
Figure 20. Transverse momentum (p_T) distribution of the final state muons at the partonic level. The blue and green colored lines correspond to the signal event generated with different Z_D masses, $M_{Z_D} = 2$, and 2.80 GeV, respectively. The orange and the brown colored line represents the p_T distribution of the $ZZ^* \to 4l$ and electroweak $4l$ background.

7.3.3 $H_2 \to \chi_+\chi_+ \to Z_D\chi_-Z_D\chi_-$

The SM-like Higgs boson, H_2, can also undergo decay into a pair of $\chi_+\chi_+$, which can result in a $4\mu + \slashed{E}_T$ final state, through cascade decay via $\chi_+\chi_+ \to (Z_D \to \mu^+\mu^-)\chi_-(Z_D \to \mu^+\mu^-)\chi_-$. In this case, χ_- constitutes a source of $\slashed{E}_T$.

In this subsection, we present a search strategy for Z_D in the $H_2 \to \chi_+\chi_+ \to Z_D\chi_-Z_D\chi_-$ channel, in context of a 14 TeV LHC with $\mathcal{L} = 3000\,\text{fb}^{-1}$. Similar to the case of section 7.3.2, we only consider the ggF mode of Higgs production. $gg \to H_2 \to \chi_+\chi_+ \to Z_D\chi_-Z_D\chi_-$ constitutes the signal, where, $gg \to H_2$ samples have been generated with MadGraph [164], while Pythia-6 [165] has been used to perform the cascade decay and showering. The benchmark point shown in table. 2, with $M_{\chi_+} = 5.8187$ GeV and $M_{\chi_-} = 2.4$ GeV, has been chosen to perform this search.

The muon isolation and selection criteria specified in section 7.3.2 is applied here as well, and an event is required to have exactly four isolated muons in the final state. We
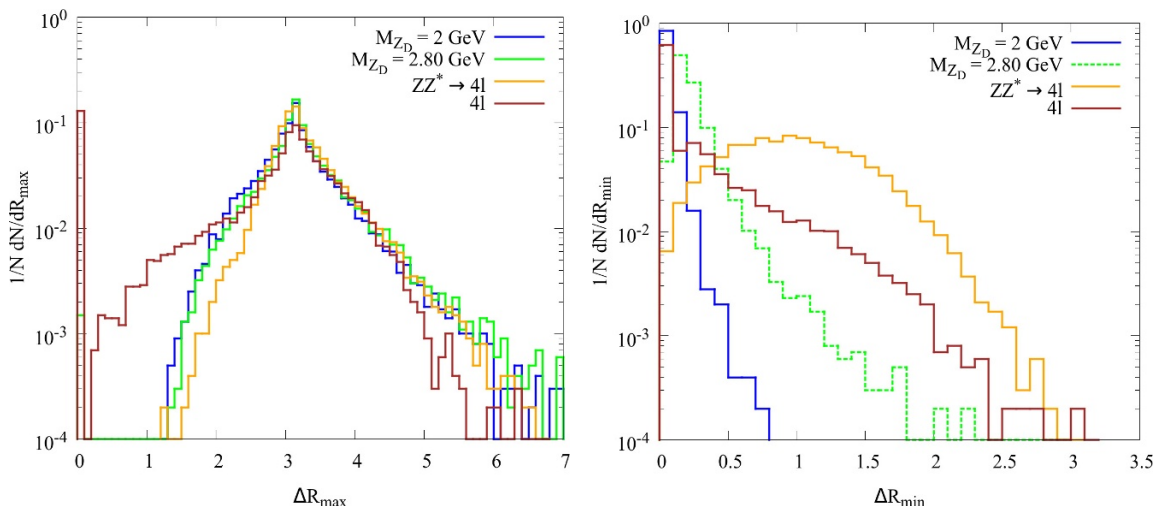
Figure 21. Normalised distribution showing $\Delta R_{\max}$ and $\Delta R_{\min}$. The color codes are the same as that of figure 20.

show the p_T distribution of the final state muons, corresponding to the relevant backgrounds (same color code as figure 17) and two benchmark signal events ($M_{Z_D} = 2.0$ GeV and $M_{Z_D} = 2.8$ GeV), in figure 20, where, p_T^1 represents the highest p_T muon and p_T^4 represents the lowest p_T muon. When compared to the case of section 7.3.2, the p_T distribution of the signal events peak at a relatively smaller value on account of a residual $\not{E}_T$. Consequently, we apply slightly weaker trigger cuts on the muon p_T. The muon with the highest p_T is required to have $p_T > 15$ GeV, while the second (third) leading muon is required to have $p_T > 10$ GeV(5 GeV). Here again, the angular variables, ΔR, provides an additional control in improving upon the signal significance. In this context, we show the $\Delta R_{\max}$ and $\Delta R_{\min}$ distributions in figure 21, following the color code of figure 20. $\Delta R_{\max}$ ($\Delta R_{\min}$) represents the maximum (minimum) value of ΔR between all possible muon pairs. It can be observed from figure 21 that the $\Delta R_{\max}$ distribution for the 4l background falls off earlier than the signal samples. Consequently, we impose $\Delta R_{\max} > 2.0$. In addition, a lower limit on $\Delta R_{\min} > 0.5$ is also imposed. The construction of SFOS pair is done following the strategy specified in section 7.3.2. An event is required to have exactly two SFOS pairs, with the invariant mass of the leading and sub-leading SFOS pairs required to be within the range 0.88 GeV $< M_{12}, M_{34} < 20$ GeV. The ratio of invariant masses of the sub-leading and leading SFOS pair is required to be within $\dfrac{M_{34}}{M_{12}} > 0.85$. The J/Ψ and Υ resonance vetoes have also been applied in this analysis. A summary of selection cuts is presented in table. 5. The HL-LHC upper limits on $\sigma(gg \to H_2) \times Br(H_2 \to \chi_+\chi_+ \to \chi_- Z_D \chi_- Z_D)$ corresponding to a signal significance of 5σ and 2σ are shown in table. 6. For the sake of comparison, the upper limits on $\sigma(gg \to H_2 \to Z_D Z_D)$, derived in section 7.3.2, are also shown in the same table.

The case of $H_2 \to Z_D Z_D$ (discussed in section 7.3.2), furnishes stronger limits as compared to the current case, and the reason can be attributed to the possibility of invariant mass reconstruction of H_2 ($M_{4\mu}$) in the previous case. We would like to note that in the case of $H_2 \to Z_D Z_D$, we had imposed a selection cut on $M_{4\mu}$ and had restricted it within $120 - 130$ GeV, which was extremely efficient in filtering out the background.

Selection cuts
(a). Exactly 4 muons in final state.
(b). $p_T^{\mu_1} > 15$ GeV, $p_T^{\mu_2} > 10$ GeV
$p_T^{\mu_3} > 5$ GeV, $p_T^{\mu_4} > 2.6$ GeV
$\lvert \eta \rvert < 4$
(c). $\Delta R_{\max} > 2.0$ and $\Delta R_{\min} > 0.5$
(d). 0.88 GeV $< M_{12}^{inv}, M_{34}^{inv} < 20$ GeV
(e). Event veto if: $(M_{J/\Psi} - 0.25$ GeV$) < M_{12,34} < (M_{\Psi(2s)} + 0.30$ GeV$)$
$(M_\Upsilon - 0.70$ GeV$) < M_{12,34} < (M_{\Upsilon(3s)} + 0.75$ GeV$)$
(f). $M_{34}^{inv}/M_{12}^{inv} > 0.85$

Table 5. Selection cuts for the cut-based analysis in the $4\mu + \not{E}_T$ final state.

| M_{Z_D} [GeV]	$H_2 \rightarrow \chi_+\chi_+ \rightarrow 4\mu + \not{E}_T$		$H_2 \rightarrow Z_D Z_D \rightarrow 4\mu$	
	5σ [fb]	2σ [fb]	5σ [fb]	2σ [fb]
2.40	1.03	0.41	0.181	0.072

Table 6. Upper limits corresponding to 5σ and 2σ signal significances on $\sigma(gg \rightarrow H_2) \times Br(H_2 \rightarrow \chi_+\chi_+ \rightarrow \chi_- Z_D \chi_- Z_D)$ for HL-LHC. The upper limits derived in section 7.3.2 for $\sigma(gg \rightarrow H_2 \rightarrow Z_D Z_D)$ are also listed.

7.3.4 The curious case of a late decaying Z_D boson at 14 TeV and 27 TeV high luminosity LHC

In the recent times, non-traditional search methodologies for beyond the Standard Models (BSM) physics have started garnering popularity. Search for the late decaying long-lived particles (LLP) which feature a characteristic secondary vertex has emerged as one such avenue. In general, a particle is said to be long-lived if its proper decay length exceeds $c\tau > 10^{-4}$ m. Z_D is one such viable LLP candidate within the framework of the U(1)$_D$ model considered in this analysis. The proper decay length of Z_D has an inverse square dependence on the kinetic mixing factor ϵ_g, and can become a potential LLP candidate for smaller values of ϵ_g. For example, at $M_{Z_D} \sim 2$ GeV, a value of $\epsilon_g \gtrsim (10^{-5} - 10^{-6})$ will result in the Z_D to become a LLP (see figure 2 of [171]).

Before proceeding ahead with the details of the analysis, we lay down a brief description of the existing segmentation of the ATLAS detector. The ATLAS detector can be broadly classified into four different segments, viz., the tracker region, the electromagnetic calorimeter (ECAL), the hadronic calorimeter (HCAL) and the muon spectrometer. The tracker region can be further subdivided into three major segments. The first segment involves the Pixel detector, which contains three sub-layers at a radii of 33.25 mm, 50.5 mm, and 88.5 mm. The next segment within the tracker is the SCT which can be further classified into three segments with radii 299 mm, 371 mm, and 443 mm. The final segment in the tracker is the TRT which spans the radii 554 mm − 1082 mm. The ECAL segment
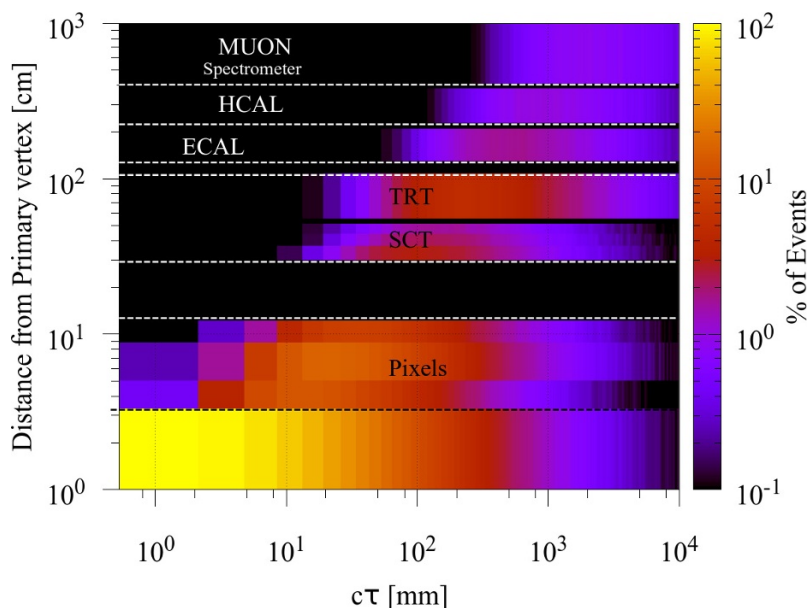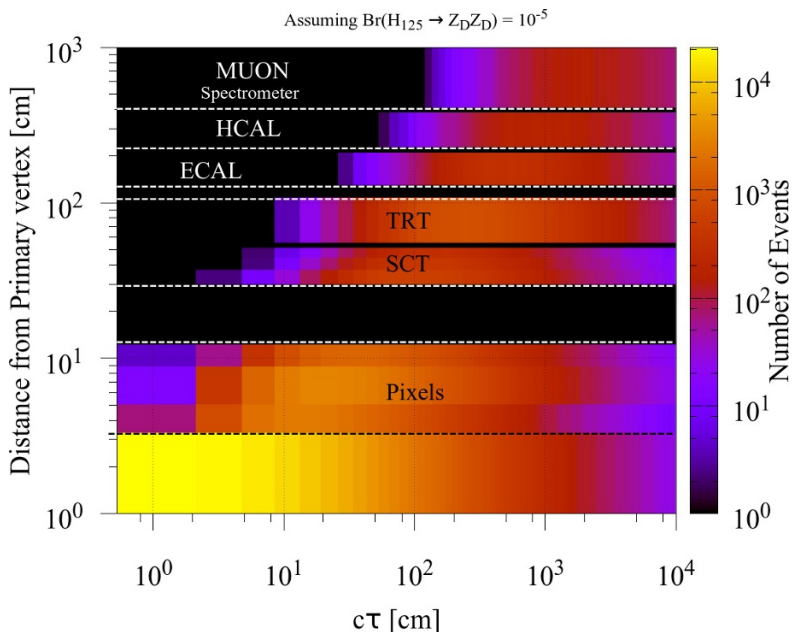
Figure 22. The vertical and horizontal axes represent the radii from the beam axis and proper decay length, respectively, of the LLP. The color palette corresponds to the percentage of events which will undergo decay in the corresponding segments, for the case of 14 TeV LHC with an integrated luminosity of $3000\,\mathrm{fb}^{-1}$. The segmentation along the vertical axis corresponds to the existing geometry of the ATLAS detector.

lies roughly in between a radii of $\sim 1300\,\mathrm{mm} - 2100\,\mathrm{mm}$, while the HCAL scans across a radii of $\sim 2285\,\mathrm{mm} - 3815\,\mathrm{mm}$. The final segment of the ATLAS detector, the muon spectrometer, extends from a radii of $\sim 4100\,\mathrm{mm}$ all the way up to $10000\,\mathrm{mm}$.

The LLP can undergo decay in different segments of the LHC, based on its kinematic distribution and its decay length. The decay length is given by $l_d = \beta\gamma c\tau$, where, β is the boost of the particle and is defined as the ratio of its velocity (v) to the speed of light (c): $\beta = v/c$, whereas, $c\tau$ is the proper lifetime of the particle in its rest frame, and γ is the relativistic factor defined as: $\gamma = \dfrac{1}{\sqrt{1-\beta^2}}$. It can be inferred from the form of the decay length that identification of the secondary vertex within the detector (which corresponds to the point of decay of the LLP) and measurement of the boost factor, can also be used to estimate the proper lifetime of the LLP. Within a typical detector, if N_0 be the number of long-lived particles produced with a proper life time τ_i and a mean life-time of τ, then the exponential distribution gives the total number of decay events, $N = N_0 e^{-\tau_i/\tau}$. Consequently, the fraction of long-lived particles undergoing decay in different segments of the detector will be a characteristic reflection of the proper decay length.

To visualize this effect, we used `Pythia-6` to simulate the signal $pp \to H_2 \to Z_D Z_D$ with Z_D being a LLP. Event samples were generated by varying the decay length of Z_D over the range from 0.5 mm to 10000 mm, and $20,000$ events were generated for specific choice of decay length. We show the proper decay length (in mm) along the horizontal axis and the radii (in cm) along the vertical axis in figure 22 (following the ATLAS detector geometry),

Figure 23. The vertical and horizontal axes represent the radii from the beam axis and proper decay length, respectively, of the LLP. The color palette corresponds to the total of events which will undergo decay in the corresponding segments, for the case of 27 TeV LHC at an integrated luminosity of 15 ab^{-1}. Here, we assume $Br(H_2 \to Z_D Z_D) = 10^{-5}$. The segmentation along the vertical axis corresponds to the existing geometry of the ATLAS detector.

with the color palettes being representative of the percentage of events decaying within the concerned segment. The black colored regions correspond to the void regions within the detector and also represents those segments which do not register an event decay. The event samples for figure 22 have been simulated for the case of 14 TeV LHC. It can be observed that particles with proper decay length up to ~ 10 cm mostly decay before reaching the Pixel detector. Particles with large proper decay length can be observed to have a fairly uniform probability of decaying throughout the detectors. We would like to note that, in order to correctly simulate the effect of a smeared distribution, we generated events with proper decay lengths up to 20000 mm and then truncated the horizontal range in figure 22 at 10000 mm. Observation of the LLP at different segments of the detector can be instrumental in motivating the design of segment-specific search analyses. Reconstruction of the same type of particle at the tracker and the ECAL involves vastly different strategies, and different search analyses would be required at these two different segments. Under such circumstances, having a generic idea about the probability of decay within a certain segment of the detector can prove instrumental in performing more specific and focused searches.

We perform a similar study for the case of a 27 TeV LHC machine as well, assuming the current geometry of ATLAS detector, and the corresponding results are represented in figure 23. Here, we show the total number of $gg \to H_2 \to Br(H_2 \to Z_D Z_D)$ events, assuming $\sigma(gg \to H_2) = 140$ pb, $Br(H_2 \to Z_D Z_D) = 10^{-5}$, and an integrated luminosity of 15 ab^{-1}, in the color palette. The horizontal and vertical axes in figure 23 correspond

Segment	Percentage of events undergoing decay					
	$c\tau = 13.2$ mm		$c\tau = 305.2$ mm		$c\tau = 1025$ mm	
	ggF	ZH_2	ggF	ZH_2	ggF	ZH_2
Prompt	52.84	48.70	3.720	3.325	1.127	1.010
Pixel	32.84	31.18	7.117	6.320	2.275	2.230
SCT	0.347	0.685	4.908	4.320	2.050	1.770
TRT	0.020	0.085	4.452	3.795	2.523	2.090
ECAL	0.002	0.000	1.442	1.215	1.290	1.030
HCAL	0.000	0.000	0.485	0.560	0.942	0.755
μ spec.	0.000	0.000	0.117	0.194	0.667	0.580

Table 7. Percentage of events undergoing decay in different segments of the detector corresponding to the ggF and ZH_2 production modes of H_2, for the case of 14 TeV LHC. The difference is the manifestation of different kinematics for the two cases.

to the similar quantities in figure 22. A higher boost in the case of 27 TeV collision results in an upward shift of color pattern in figure 23 as compared to the previous case.

The preceding discussion assumed the Higgs production in the ggF channel. The production of Higgs in other production channels will result in alteration of the segment-wise decay fraction, owing to different boosts in the transverse direction. In this respect, we briefly explore the case of ZH_2 production, and the LLP being produced from decay of H_2, in the context of 14 TeV LHC. We present a comparison between the fraction of events undergoing decay within various segments of the detector, for the case of H_2 being produced via ggF mode and in ZH_2 mode, in table. 7.

8 Summary and conclusion

In this work, we have explored an U(1)$_D$-gauge extension of Standard Model from a phenomenological perspective. Our model has two Majorana fermions to render the theory anomaly free. The lightest of them serves as a dark matter candidate. As generic to any gauge theory, our model has an extra neutral Z like boson (Z_D) and since we have also agreed to employ Higgs mechanism to make the particles massive, there also exists an extra neutral scalar (H_1) besides the usual Standard Model Higgs boson. Motivation of studying strong dark matter self-interactions led us to restrict ourselves only to light scalar mediators ($10\,\text{MeV} \lesssim M_{H_1} \lesssim 10\,\text{GeV}$). Here we have studied the specific case where Sommerfeld enhancement is mediated only through one light mediator (H_1). In general, both, Z_D and H_1, could have been light and led to large self-interactions, but very light Z_D would have been devoid of any collider signatures.

For simplicity, throughout this work we have restricted the kinetic mixing between Z and Z_D to small values. However, it plays a role in the study of collider signatures arising from the prompt decay of Z_D. The primary goal of this work was to investigate

if there exists a substantial parameter space for a thermal dark matter with large self-interactions. The latter is desirable since it solves various small scale structure issues, as already mentioned earlier. The range of M_{H_1} was hence motivated by the requirement of large self-interaction cross-sections. We have systematically checked constraints on scalar mixing angle (as a function of M_{H_1}) arising from LEP data, B-factories and beam dump experiments. We found that LEP data rules out $\sin\theta_{\mathrm{mix}} \gtrsim 0.2$ for the entire range of M_{H_1} considered in this work. Higgs signal strength measurements on the other hand constrained $\sin\theta_{\mathrm{mix}}$ to $\lesssim 0.1$ in our parameter space of interest. Beam dump and flavor physics experiments put a tighter bound of $\sin\theta_{\mathrm{mix}} \lesssim 10^{-4}$ on almost the whole of our parameter space. LHC analyses mainly dealt with Standard Model Higgs decaying to $4l$ channels and provided us with a probe to the otherwise small gauge kinetic mixing (ϵ_g).

From the point of view of dark matter phenomenology we however have the most stringent constraints on the scalar mixing angle (for a given Yukawa coupling f). The Yukawa coupling f is the sole controlling parameter that gives rise to sizeable self-interactions while direct detection experiments tend to put limits on $f\sin\theta_{\mathrm{mix}}$. Due to the presence of light mediators (H_1), the standard calculation of DM-nucleon cross-section had to be refined using momentum dependent propagators. On the other hand, we have shown that the condition of thermalization of the dark and visible sectors sets a lower limit to λ_{mix}. This competes with the upper bound on λ_{mix} that arises from the direct detection experiments (for a given v_D and a suitable f which will give rise to sizeable self-interactions). Our findings suggest that such points on the parameter space satisfying both the limits are very rare and generally prefers low dark matter masses ($\sim \mathcal{O}(1)$) GeV where constraints from direct detection is considerably weaker. Alternatively, we can also try to do away with the usual *thermal* dark matter scenario and probe into other exotic mechanisms like dark freeze-out [172] and freeze-in [173–177] to achieve the correct relic density, although the latter requires substantially small portal couplings and would be difficult to probe. λ_{mix} will have no lower limit in these cases and hence a large portion of the parameter space can be recovered.

As discussed earlier, we find that it is difficult to probe the MeV scale dark H_1 in our model via future collider experiments. However, the dark gauge boson Z_D may be probed at future HL-LHC. We have presented the reach of Z_D from H_2 decay via 4μ final state and obtained projected upper limits on $\sigma_{H_2} \times Br(H_2 \to Z_D Z_D)$ for HL-LHC. We have also looked into the scenario where H_2 decays into a pair of χ_+ ($\chi_+ \to Z_D\chi_-$) and finally results into $4\mu+$ MET signal and found that this channel gives weaker limit compared to $H_2 \to Z_D Z_D \to 4\mu$ channel. For very small values of ϵ_g, Z_D becomes a long lived particle (LLP) and different search strategies are required for the LLP scenarios. This non-traditional prospects of LLP (Z_D) at 14 TeV and 27 TeV high luminosity LHC have also been discussed.

Thus, solely from a data driven perspective, in a general and minimal U(1)-gauge extension of Standard Model, we were able to restrict the presence of a *heavy thermal* dark matter candidate and this motivates (quantitatively) future explorations along these uncharted avenues.

Acknowledgments

References

[1] G. Bertone, *Particle dark matter: observations, models and searches*, Cambridge Univ. Press, Cambridge, U.K. (2010) [INSPIRE].

[2] PLANCK collaboration, *Planck 2018 results. VI. Cosmological parameters*, arXiv:1807.06209 [INSPIRE].

[3] PLANCK collaboration, *Planck 2015 results. XIII. Cosmological parameters*, *Astron. Astrophys.* **594** (2016) A13 [arXiv:1502.01589] [INSPIRE].

[4] B. Carr, F. Kuhnel and M. Sandstad, *Primordial black holes as dark matter*, *Phys. Rev.* **D 94** (2016) 083504 [arXiv:1607.06077] [INSPIRE].

[5] S. Clark, B. Dutta, Y. Gao, Y.-Z. Ma and L.E. Strigari, 21 *cm limits on decaying dark matter and primordial black holes*, *Phys. Rev.* **D 98** (2018) 043006 [arXiv:1803.09390] [INSPIRE].

[6] H. Niikura et al., *Microlensing constraints on primordial black holes with the Subaru/HSC Andromeda observation*, arXiv:1701.02151 [INSPIRE].

[7] M. Drees and E. Erfani, *Running spectral index and formation of primordial black hole in single field inflation models*, *JCAP* **01** (2012) 035 [arXiv:1110.6052] [INSPIRE].

[8] M. Drees and E. Erfani, *Running-mass inflation model and primordial black holes*, *JCAP* **04** (2011) 005 [arXiv:1102.2340] [INSPIRE].

[9] G. Jungman, M. Kamionkowski and K. Griest, *Supersymmetric dark matter*, *Phys. Rept.* **267** (1996) 195 [hep-ph/9506380] [INSPIRE].

[10] G. Bertone, D. Hooper and J. Silk, *Particle dark matter: evidence, candidates and constraints*, *Phys. Rept.* **405** (2005) 279 [hep-ph/0404175] [INSPIRE].

[11] MAGIC collaboration, *Constraining dark matter lifetime with a deep gamma-ray survey of the Perseus galaxy cluster with MAGIC*, *Phys. Dark Univ.* **22** (2018) 38 [arXiv:1806.11063] [INSPIRE].

[12] T. Cohen, K. Murase, N.L. Rodd, B.R. Safdi and Y. Soreq, γ-*ray constraints on decaying dark matter and implications for IceCube*, *Phys. Rev. Lett.* **119** (2017) 021102 [arXiv:1612.05638] [INSPIRE].

[13] M. Cirelli, E. Moulin, P. Panci, P.D. Serpico and A. Viana, γ-*ray constraints on decaying dark matter*, *Phys. Rev.* **D 86** (2012) 083506 [arXiv:1205.5283] [INSPIRE].

[14] T.R. Slatyer and C.-L. Wu, *General constraints on dark matter decay from the cosmic microwave background*, *Phys. Rev.* **D 95** (2017) 023010 [`arXiv:1610.06933`] [ɪɴSPIRE].

[15] R. Kallosh, A.D. Linde, D.A. Linde and L. Susskind, *Gravity and global symmetries*, *Phys. Rev.* **D 52** (1995) 912 [`hep-th/9502069`] [ɪɴSPIRE].

[16] T. Banks, M. Johnson and A. Shomer, *A note on gauge theories coupled to gravity*, *JHEP* **09** (2006) 049 [`hep-th/0606277`] [ɪɴSPIRE].

[17] J. Berger, K. Jedamzik and D.G.E. Walker, *Cosmological constraints on decoupled dark photons and dark Higgs*, *JCAP* **11** (2016) 032 [`arXiv:1605.07195`] [ɪɴSPIRE].

[18] Y. Mambrini, S. Profumo and F.S. Queiroz, *Dark matter and global symmetries*, *Phys. Lett.* **B 760** (2016) 807 [`arXiv:1508.06635`] [ɪɴSPIRE].

[19] X. Chu and B. Dasgupta, *Dark radiation alleviates problems with dark matter halos*, *Phys. Rev. Lett.* **113** (2014) 161301 [`arXiv:1404.6127`] [ɪɴSPIRE].

[20] P. Ko and T. Nomura, *Phenomenology of dark matter in chiral* $U(1)_X$ *dark sector*, *Phys. Rev.* **D 94** (2016) 115015 [`arXiv:1607.06218`] [ɪɴSPIRE].

[21] C. Garcia-Cely, A. Ibarra and E. Molinaro, *Cosmological and astrophysical signatures of dark matter annihilations into pseudo-Goldstone bosons*, *JCAP* **02** (2014) 032 [`arXiv:1312.3578`] [ɪɴSPIRE].

[22] C. Garcia-Cely, A. Ibarra and E. Molinaro, *Dark matter production from Goldstone boson interactions and implications for direct searches and dark radiation*, *JCAP* **11** (2013) 061 [`arXiv:1310.6256`] [ɪɴSPIRE].

[23] N. Okada and O. Seto, *Higgs portal dark matter in the minimal gauged* $U(1)_{B-L}$ *model*, *Phys. Rev.* **D 82** (2010) 023507 [`arXiv:1002.2525`] [ɪɴSPIRE].

[24] X.-G. He, G.C. Joshi, H. Lew and R.R. Volkas, *Simplest* Z' *model*, *Phys. Rev.* **D 44** (1991) 2118 [ɪɴSPIRE].

[25] X.G. He, G.C. Joshi, H. Lew and R.R. Volkas, *New* Z' *phenomenology*, *Phys. Rev.* **D 43** (1991) 22 [ɪɴSPIRE].

[26] S. Matsumoto, Y.-L.S. Tsai and P.-Y. Tseng, *Light fermionic WIMP dark matter with light scalar mediator*, [`arXiv:1811.03292`] [ɪɴSPIRE].

[27] CMS collaboration, *Search for associated production of dark matter with a Higgs boson decaying to* $b\bar{b}$ *or* $\gamma\gamma$ *at* $\sqrt{s} = 13\,TeV$, *JHEP* **10** (2017) 180 [`arXiv:1703.05236`] [ɪɴSPIRE].

[28] ATLAS collaboration, *Search for dark matter in association with a Higgs boson decaying to b-quarks in pp collisions at* $\sqrt{s} = 13\,TeV$ *with the ATLAS detector*, *Phys. Lett.* **B 765** (2017) 11 [`arXiv:1609.04572`] [ɪɴSPIRE].

[29] CMS collaboration, *Search for new physics in dijet angular distributions using proton-proton collisions at* $\sqrt{s} = 13\,TeV$ *and constraints on dark matter and other models*, *Eur. Phys. J.* **C 78** (2018) 789 [`arXiv:1803.08030`] [ɪɴSPIRE].

[30] XENON collaboration, *Dark matter search results from a one ton-year exposure of XENON1T*, *Phys. Rev. Lett.* **121** (2018) 111302 [`arXiv:1805.12562`] [ɪɴSPIRE].

[31] LUX collaboration, *Results from a search for dark matter in the complete LUX exposure*, *Phys. Rev. Lett.* **118** (2017) 021303 [`arXiv:1608.07648`] [ɪɴSPIRE].

[32] PandaX-II collaboration, *Dark matter results from 54-ton-day exposure of PandaX-II experiment*, *Phys. Rev. Lett.* **119** (2017) 181302 [`arXiv:1708.06917`] [ɪɴSPIRE].

[33] FERMI-LAT and DES collaborations, *Searching for dark matter annihilation in recently discovered milky way satellites with Fermi-LAT*, *Astrophys. J.* **834** (2017) 110 [arXiv:1611.03184] [INSPIRE].

[34] AMS collaboration, *Antiproton flux, antiproton-to-proton flux ratio and properties of elementary particle fluxes in primary cosmic rays measured with the Alpha Magnetic Spectrometer on the International Space Station*, *Phys. Rev. Lett.* **117** (2016) 091103 [INSPIRE].

[35] D.H. Weinberg, J.S. Bullock, F. Governato, R. Kuzio de Naray and A.H.G. Peter, *Cold dark matter: controversies on small scales*, *Proc. Nat. Acad. Sci.* **112** (2015) 12249 [arXiv:1306.0913] [INSPIRE].

[36] P. Bull et al., *Beyond ΛCDM: problems, solutions and the road ahead*, *Phys. Dark Univ.* **12** (2016) 56 [arXiv:1512.05356] [INSPIRE].

[37] A. Del Popolo and M. Le Delliou, *Small scale problems of the ΛCDM model: a short review*, *Galaxies* **5** (2017) 17 [arXiv:1606.07790] [INSPIRE].

[38] B. Moore, *Evidence against dissipationless dark matter from observations of galaxy haloes*, *Nature* **370** (1994) 629 [INSPIRE].

[39] R.A. Flores and J.R. Primack, *Observational and theoretical constraints on singular dark matter halos*, *Astrophys. J.* **427** (1994) L1 [astro-ph/9402004] [INSPIRE].

[40] M. Boylan-Kolchin, J.S. Bullock and M. Kaplinghat, *Too big to fail? The puzzling darkness of massive milky way subhaloes*, *Mon. Not. Roy. Astron. Soc.* **415** (2011) L40 [arXiv:1103.0007] [INSPIRE].

[41] I. Ferrero, M.G. Abadi, J.F. Navarro, L.V. Sales and S. Gurovich, *The dark matter halos of dwarf galaxies: a challenge for the ΛCDM paradigm?*, *Mon. Not. Roy. Astron. Soc.* **425** (2012) 2817 [arXiv:1111.6609] [INSPIRE].

[42] S. Garrison-Kimmel, M. Boylan-Kolchin, J.S. Bullock and E.N. Kirby, *Too big to fail in the local group*, *Mon. Not. Roy. Astron. Soc.* **444** (2014) 222 [arXiv:1404.5313] [INSPIRE].

[43] E. Papastergis, R. Giovanelli, M.P. Haynes and F. Shankar, *Is there a "too big to fail" problem in the field?*, *Astron. Astrophys.* **574** (2015) A113 [arXiv:1407.4665] [INSPIRE].

[44] A.A. Klypin, A.V. Kravtsov, O. Valenzuela and F. Prada, *Where are the missing galactic satellites?*, *Astrophys. J.* **522** (1999) 82 [astro-ph/9901240] [INSPIRE].

[45] B. Moore et al., *Dark matter substructure within galactic halos*, *Astrophys. J.* **524** (1999) L19 [astro-ph/9907411] [INSPIRE].

[46] E.J. Tollerud, J.S. Bullock, L.E. Strigari and B. Willman, *Hundreds of milky way satellites? Luminosity bias in the satellite luminosity function*, *Astrophys. J.* **688** (2008) 277 [arXiv:0806.4381] [INSPIRE].

[47] S. Walsh, B. Willman and H. Jerjen, *The invisibles: a detection algorithm to trace the faintest milky way satellites*, *Astron. J.* **137** (2009) 450 [arXiv:0807.3345] [INSPIRE].

[48] D.N. Spergel and P.J. Steinhardt, *Observational evidence for selfinteracting cold dark matter*, *Phys. Rev. Lett.* **84** (2000) 3760 [astro-ph/9909386] [INSPIRE].

[49] R. Dave, D.N. Spergel, P.J. Steinhardt and B.D. Wandelt, *Halo properties in cosmological simulations of selfinteracting cold dark matter*, *Astrophys. J.* **547** (2001) 574 [astro-ph/0006218] [INSPIRE].

[50] S. Tulin and H.-B. Yu, *Dark matter self-interactions and small scale structure*, *Phys. Rept.* **730** (2018) 1 [arXiv:1705.02358] [INSPIRE].

[51] S. Tulin, H.-B. Yu and K.M. Zurek, *Beyond collisionless dark matter: particle physics dynamics for dark matter halo structure*, *Phys. Rev.* **D 87** (2013) 115007 [arXiv:1302.3898] [INSPIRE].

[52] M. Rocha et al., *Cosmological simulations with self-interacting dark matter I: constant density cores and substructure*, *Mon. Not. Roy. Astron. Soc.* **430** (2013) 81 [arXiv:1208.3025] [INSPIRE].

[53] A.H.G. Peter, M. Rocha, J.S. Bullock and M. Kaplinghat, *Cosmological simulations with self-interacting dark matter II: halo shapes vs. observations*, *Mon. Not. Roy. Astron. Soc.* **430** (2013) 105 [arXiv:1208.3026] [INSPIRE].

[54] J. Zavala, M. Vogelsberger and M.G. Walker, *Constraining self-interacting dark matter with the milky way's dwarf spheroidals*, *Mon. Not. Roy. Astron. Soc.* **431** (2013) L20 [arXiv:1211.6426] [INSPIRE].

[55] O.D. Elbert, J.S. Bullock, S. Garrison-Kimmel, M. Rocha, J. Oñorbe and A.H.G. Peter, *Core formation in dwarf haloes with self-interacting dark matter: no fine-tuning necessary*, *Mon. Not. Roy. Astron. Soc.* **453** (2015) 29 [arXiv:1412.1477] [INSPIRE].

[56] M. Markevitch et al., *Direct constraints on the dark matter self-interaction cross-section from the merging galaxy cluster* 1E0657-56, *Astrophys. J.* **606** (2004) 819 [astro-ph/0309303] [INSPIRE].

[57] D. Clowe, A. Gonzalez and M. Markevitch, *Weak lensing mass reconstruction of the interacting cluster* 1E0657-558*: direct evidence for the existence of dark matter*, *Astrophys. J.* **604** (2004) 596 [astro-ph/0312273] [INSPIRE].

[58] S.W. Randall, M. Markevitch, D. Clowe, A.H. Gonzalez and M. Bradac, *Constraints on the self-interaction cross-section of dark matter from numerical simulations of the merging galaxy cluster* 1E0657-56, *Astrophys. J.* **679** (2008) 1173 [arXiv:0704.0261] [INSPIRE].

[59] R. Massey et al., *The behaviour of dark matter associated with four bright cluster galaxies in the* 10 *kpc core of Abell* 3827, *Mon. Not. Roy. Astron. Soc.* **449** (2015) 3393 [arXiv:1504.03388] [INSPIRE].

[60] F. Kahlhoefer, K. Schmidt-Hoberg, J. Kummer and S. Sarkar, *On the interpretation of dark matter self-interactions in Abell* 3827, *Mon. Not. Roy. Astron. Soc.* **452** (2015) L54 [arXiv:1504.06576] [INSPIRE].

[61] R. Massey et al., *Dark matter dynamics in Abell* 3827*: new data consistent with standard cold dark matter*, *Mon. Not. Roy. Astron. Soc.* **477** (2018) 669 [arXiv:1708.04245] [INSPIRE].

[62] M. Kaplinghat, S. Tulin and H.-B. Yu, *Dark matter halos as particle colliders: unified solution to small-scale structure puzzles from dwarfs to clusters*, *Phys. Rev. Lett.* **116** (2016) 041302 [arXiv:1508.03339] [INSPIRE].

[63] J. Hisano, S. Matsumoto, M.M. Nojiri and O. Saito, *Non-perturbative effect on dark matter annihilation and gamma ray signature from galactic center*, *Phys. Rev.* **D 71** (2005) 063528 [hep-ph/0412403] [INSPIRE].

[64] M. Cirelli, A. Strumia and M. Tamburini, *Cosmology and astrophysics of minimal dark matter*, *Nucl. Phys.* **B 787** (2007) 152 [arXiv:0706.4071] [INSPIRE].

[65] N. Arkani-Hamed, D.P. Finkbeiner, T.R. Slatyer and N. Weiner, *A theory of dark matter*, *Phys. Rev.* **D 79** (2009) 015014 [`arXiv:0810.0713`] [InSPIRE].

[66] J.L. Feng, M. Kaplinghat and H.-B. Yu, *Halo shape and relic density exclusions of Sommerfeld-enhanced dark matter explanations of cosmic ray excesses*, *Phys. Rev. Lett.* **104** (2010) 151301 [`arXiv:0911.0422`] [InSPIRE].

[67] E.C.G. Stueckelberg, *Die Wechselwirkungs Kraefte in der Elektrodynamik und in der Feldtheorie der Kernkraefte (I)* (in German), *Helv. Phys. Acta* **11** (1938) 225 [InSPIRE].

[68] E.C.G. Stueckelberg, *Die Wechselwirkungs Kraefte in der Elektrodynamik und in der Feldtheorie der Kernkraefte (II)* (in German), *Helv. Phys. Acta* **11** (1938) 299 [InSPIRE].

[69] E.C. Stueckelberg, *Die Wechselwirkungs Kraefte in der Elektrodynamik und in der Feldtheorie der Kernkraefte (III)* (in German), *Helv. Phys. Acta* **11** (1938) 312.

[70] V.I. Ogievetskii and I.V. Polubarinov, *A gauge invariant formulation of neutral vector field theory*, *JETP* **14** (1962) 179.

[71] B. Holdom, *Two* U(1)*'s and epsilon charge shifts*, *Phys. Lett.* **B 166** (1986) 196 [InSPIRE].

[72] R.M. Fonseca, M. Malinsky, W. Porod and F. Staub, *Running soft parameters in SUSY models with multiple* U(1) *gauge factors*, *Nucl. Phys.* **B 854** (2012) 28 [`arXiv:1107.2670`] [InSPIRE].

[73] B. O'Leary, W. Porod and F. Staub, *Mass spectrum of the minimal SUSY B-L model*, *JHEP* **05** (2012) 042 [`arXiv:1112.4600`] [InSPIRE].

[74] W. Porod, *SPheno, a program for calculating supersymmetric spectra, SUSY particle decays and SUSY particle production at e^+e^- colliders*, *Comput. Phys. Commun.* **153** (2003) 275 [`hep-ph/0301101`] [InSPIRE].

[75] W. Porod and F. Staub, *SPheno 3.1: extensions including flavour, CP-phases and models beyond the MSSM*, *Comput. Phys. Commun.* **183** (2012) 2458 [`arXiv:1104.1573`] [InSPIRE].

[76] K.S. Babu, C.F. Kolda and J. March-Russell, *Implications of generalized Z-Z' mixing*, *Phys. Rev.* **D 57** (1998) 6788 [`hep-ph/9710441`] [InSPIRE].

[77] M. Williams, C.P. Burgess, A. Maharana and F. Quevedo, *New constraints (and motivations) for Abelian gauge bosons in the MeV-TeV mass range*, *JHEP* **08** (2011) 106 [`arXiv:1103.4556`] [InSPIRE].

[78] S.A. Khrapak, A.V. Ivlev, G.E. Morfill and S.K. Zhdanov, *Scattering in the attractive Yukawa potential in the limit of strong interaction*, *Phys. Rev. Lett.* **90** (2003) 225002 [InSPIRE].

[79] S.A. Khrapak, A.V. Ivlev and G.E. Morfill, *Momentum transfer in complex plasmas*, *Phys. Rev.* **E 70** (2004) 056405.

[80] S. Tulin, H.-B. Yu and K.M. Zurek, *Beyond collisionless dark matter: particle physics dynamics for dark matter halo structure*, *Phys. Rev.* **D 87** (2013) 115007 [`arXiv:1302.3898`] [InSPIRE].

[81] M. Vogelsberger, J. Zavala and A. Loeb, *Subhaloes in self-interacting galactic dark matter haloes*, *Mon. Not. Roy. Astron. Soc.* **423** (2012) 3740 [`arXiv:1201.5892`] [InSPIRE].

[82] A. Loeb and N. Weiner, *Cores in dwarf galaxies from dark matter with a Yukawa potential*, *Phys. Rev. Lett.* **106** (2011) 171302 [`arXiv:1011.6374`] [InSPIRE].

[83] G. Mangano and P.D. Serpico, *A robust upper limit on N_{eff} from BBN, circa* 2011, *Phys. Lett.* **B 701** (2011) 296 [arXiv:1103.1261] [INSPIRE].

[84] R.H. Cyburt, B.D. Fields, K.A. Olive and T.-H. Yeh, *Big bang nucleosynthesis:* 2015, *Rev. Mod. Phys.* **88** (2016) 015004 [arXiv:1505.01076] [INSPIRE].

[85] ATLAS and CMS collaborations, *Combined measurement of the Higgs boson mass in pp collisions at $\sqrt{s} = 7$ and 8 TeV with the ATLAS and CMS experiments*, *Phys. Rev. Lett.* **114** (2015) 191803 [arXiv:1503.07589] [INSPIRE].

[86] DELPHI collaboration, *Searches for neutral Higgs bosons in e^+e^- collisions from $\sqrt{s} = 191.6$ GeV to 201.7 GeV*, *Eur. Phys. J.* **C 23** (2002) 409 [hep-ex/0201022] [INSPIRE].

[87] OPAL collaboration, *Decay mode independent searches for new scalar bosons with the OPAL detector at LEP*, *Eur. Phys. J.* **C 27** (2003) 311 [hep-ex/0206022] [INSPIRE].

[88] DELPHI collaboration, *Search for low mass Higgs bosons produced in Z^0 decays*, *Z. Phys.* **C 51** (1991) 25 [INSPIRE].

[89] DELPHI collaboration, *Search for light neutral Higgs particles produced in Z^0 decays*, *Nucl. Phys.* **B 342** (1990) 1 [INSPIRE].

[90] ALEPH, DELPHI, L3, OPAL and LEP WORKING GROUP FOR HIGGS BOSON SEARCHES collaborations, *Search for neutral MSSM Higgs bosons at LEP*, *Eur. Phys. J.* **C 47** (2006) 547 [hep-ex/0602042] [INSPIRE].

[91] J.F. Gunion, S. Dawson, H.E. Haber and G.L. Kane, *The Higgs hunter's guide*, vol. 80, Brookhaven Nat. Lab., Upton, NY, U.S.A. (1989) [*Front. Phys.* **80** (2000) 1] [INSPIRE].

[92] J. Berger, K. Jedamzik and D.G.E. Walker, *Cosmological constraints on decoupled dark photons and dark Higgs*, *JCAP* **11** (2016) 032 [arXiv:1605.07195] [INSPIRE].

[93] B. Bhattacherjee, A. Chakraborty and A. Choudhury, *Status of the MSSM Higgs sector using global analysis and direct search bounds and future prospects at the High Luminosity LHC*, *Phys. Rev.* **D 92** (2015) 093007 [arXiv:1504.04308] [INSPIRE].

[94] R.K. Barman, B. Bhattacherjee, A. Choudhury, D. Chowdhury, J. Lahiri and S. Ray, *Current status of MSSM Higgs sector with LHC 13 TeV data*, *Eur. Phys. J. Plus* **134** (2019) 150 [arXiv:1608.02573] [INSPIRE].

[95] ATLAS collaboration, *Search for Higgs boson decays to beyond-the-Standard-Model light bosons in four-lepton events with the ATLAS detector at $\sqrt{s} = 13$ TeV*, *JHEP* **06** (2018) 166 [arXiv:1802.03388] [INSPIRE].

[96] ATLAS collaboration, *Search for Higgs boson decays into a pair of light bosons in the $bb\mu\mu$ final state in pp collision at $\sqrt{s} = 13$ TeV with the ATLAS detector*, *Phys. Lett.* **B 790** (2019) 1 [arXiv:1807.00539] [INSPIRE].

[97] ATLAS collaboration, *Search for the Higgs boson produced in association with a vector boson and decaying into two spin-zero particles in the $H \to aa \to 4b$ channel in pp collisions at $\sqrt{s} = 13$ TeV with the ATLAS detector*, *JHEP* **10** (2018) 031 [arXiv:1806.07355] [INSPIRE].

[98] CMS collaboration, *A search for pair production of new light bosons decaying into muons at $\sqrt{s} = 13$ TeV*, CMS-PAS-HIG-18-003, CERN, Geneva, Switzerland (2018).

[99] CMS collaboration, *Search for an exotic decay of the Higgs boson to a pair of light pseudoscalars in the final state with two b quarks and two τ leptons in proton-proton collisions at $\sqrt{s} = 13\,TeV$, Phys. Lett.* **B 785** (2018) 462 [arXiv:1805.10191] [INSPIRE].

[100] CMS collaboration, *Search for an exotic decay of the Higgs boson to a pair of light pseudoscalars in the final state of two muons and two τ leptons in proton-proton collisions at $\sqrt{s} = 13\,TeV$, JHEP* **11** (2018) 018 [arXiv:1805.04865] [INSPIRE].

[101] CMS collaboration, *Search for light bosons in decays of the $125\,GeV$ Higgs boson in proton-proton collisions at $\sqrt{s} = 8\,TeV$, JHEP* **10** (2017) 076 [arXiv:1701.02032] [INSPIRE].

[102] ATLAS collaboration, *Search for Higgs bosons decaying to aa in the $\mu\mu\tau\tau$ final state in pp collisions at $\sqrt{s} = 8\,TeV$ with the ATLAS experiment, Phys. Rev.* **D 92** (2015) 052002 [arXiv:1505.01609] [INSPIRE].

[103] ATLAS collaboration, *Search for new light gauge bosons in Higgs boson decays to four-lepton final states in pp collisions at $\sqrt{s} = 8\,TeV$ with the ATLAS detector at the LHC, Phys. Rev.* **D 92** (2015) 092001 [arXiv:1505.07645] [INSPIRE].

[104] CMS collaboration, *A search for pair production of new light bosons decaying into muons, Phys. Lett.* **B 752** (2016) 146 [arXiv:1506.00424] [INSPIRE].

[105] CMS collaboration, *Search for a very light NMSSM Higgs boson produced in decays of the $125\,GeV$ scalar boson and decaying into τ leptons in pp collisions at $\sqrt{s} = 8\,TeV$, JHEP* **01** (2016) 079 [arXiv:1510.06534] [INSPIRE].

[106] CMS collaboration, *Search for Higgs decays to new light bosons in boosted tau final states,* CMS-PAS-HIG-14-022, CERN, Geneva, Switzerland (2015).

[107] CMS collaboration, *Search for exotic decays of the Higgs boson to a pair of new light bosons with two muon and two b jets in final states,* CMS-PAS-HIG-14-041, CERN, Geneva, Switzerland (2016).

[108] LHCb collaboration, *Search for dark photons produced in $13\,TeV$ pp collisions, Phys. Rev. Lett.* **120** (2018) 061801 [arXiv:1710.02867] [INSPIRE].

[109] BaBar collaboration, *Search for invisible decays of a dark photon produced in e^+e^- collisions at BaBar, Phys. Rev. Lett.* **119** (2017) 131804 [arXiv:1702.03327] [INSPIRE].

[110] KLOE-2 collaboration, *Search for a vector gauge boson in ϕ meson decays with the KLOE detector, Phys. Lett.* **B 706** (2012) 251 [arXiv:1110.0411] [INSPIRE].

[111] H. Merkel et al., *Search at the Mainz microtron for light massive gauge bosons relevant for the muon $g-2$ anomaly, Phys. Rev. Lett.* **112** (2014) 221802 [arXiv:1404.5502] [INSPIRE].

[112] NA64 collaboration, *Search for vector mediator of dark matter production in invisible decay mode, Phys. Rev.* **D 97** (2018) 072002 [arXiv:1710.00971] [INSPIRE].

[113] E.M. Riordan et al., *A search for short lived axions in an electron beam dump experiment, Phys. Rev. Lett.* **59** (1987) 755 [INSPIRE].

[114] A. Bross, M. Crisler, S.H. Pordes, J. Volk, S. Errede and J. Wrbanek, *A search for shortlived particles produced in an electron beam dump, Phys. Rev. Lett.* **67** (1991) 2942 [INSPIRE].

[115] A. Konaka et al., *Search for neutral particles in electron beam dump experiment, Phys. Rev. Lett.* **57** (1986) 659 [INSPIRE].

[116] HADES collaboration, *Searching a dark photon with HADES*, *Phys. Lett.* **B 731** (2014) 265 [arXiv:1311.0216] [InSPIRE].

[117] MiniBooNE collaboration, *Dark matter search in a proton beam dump with MiniBooNE*, *Phys. Rev. Lett.* **118** (2017) 221803 [arXiv:1702.02688] [InSPIRE].

[118] J. Balewski et al., *The DarkLight experiment: a precision search for new physics at low energies*, arXiv:1412.4717 [InSPIRE].

[119] J. Beacham, *APEX: A Prime EXperiment at Jefferson Lab*, in 8ᵗʰ *Patras Workshop on Axions, WIMPs and WISPs (AXION-WIMP* 2012*)*, Chicago, IL, U.S.A. 18–22 July 2012 [arXiv:1301.2581] [InSPIRE].

[120] BNL-E949 collaboration, *Study of the decay $K^+ \to \pi^+ \nu\bar{\nu}$ in the momentum region $140 < P_\pi < 199\,MeV/c$*, *Phys. Rev.* **D 79** (2009) 092004 [arXiv:0903.0030] [InSPIRE].

[121] CHARM collaboration, *Search for axion like particle production in $400\,GeV$ proton-copper interactions*, *Phys. Lett.* **B 157** (1985) 458 [InSPIRE].

[122] SuperCDMS collaboration, *Search for low-mass weakly interacting massive particles with SuperCDMS*, *Phys. Rev. Lett.* **112** (2014) 241302 [arXiv:1402.7137] [InSPIRE].

[123] LHCb collaboration, *Search for hidden-sector bosons in $B^0 \to K^{*0}\mu^+\mu^-$ decays*, *Phys. Rev. Lett.* **115** (2015) 161802 [arXiv:1508.04094] [InSPIRE].

[124] Belle collaboration, *Measurement of the differential branching fraction and forward-backword asymmetry for $B \to K^{(*)}\ell^+\ell^-$*, *Phys. Rev. Lett.* **103** (2009) 171801 [arXiv:0904.0770] [InSPIRE].

[125] Belle collaboration, *Search for $B \to h^{(*)}\nu\bar{\nu}$ decays at Belle*, *Phys. Rev. Lett.* **99** (2007) 221802 [arXiv:0707.0138] [InSPIRE].

[126] SHiP collaboration, *Sensitivity of the SHiP experiment to a light scalar particle mixing with the Higgs*, CERN-SHiP-NOTE-2017-001, CERN, Geneva, Switzerland (2017).

[127] T. Flacke, C. Frugiuele, E. Fuchs, R.S. Gupta and G. Perez, *Phenomenology of relaxion-Higgs mixing*, *JHEP* **06** (2017) 050 [arXiv:1610.02025] [InSPIRE].

[128] T. Bringmann, F. Kahlhoefer, K. Schmidt-Hoberg and P. Walia, *Strong constraints on self-interacting dark matter with light mediators*, *Phys. Rev. Lett.* **118** (2017) 141802 [arXiv:1612.00845] [InSPIRE].

[129] T. Bringmann, F. Kahlhoefer, K. Schmidt-Hoberg and P. Walia, *Converting nonrelativistic dark matter to radiation*, *Phys. Rev.* **D 98** (2018) 023543 [arXiv:1803.03644] [InSPIRE].

[130] M. Kawasaki and T. Moroi, *Electromagnetic cascade in the early universe and its application to the big bang nucleosynthesis*, *Astrophys. J.* **452** (1995) 506 [astro-ph/9412055] [InSPIRE].

[131] V. Poulin and P.D. Serpico, *Nonuniversal BBN bounds on electromagnetically decaying particles*, *Phys. Rev.* **D 91** (2015) 103007 [arXiv:1503.04852] [InSPIRE].

[132] L. Forestell, D.E. Morrissey and G. White, *Limits from BBN on light electromagnetic decays*, *JHEP* **01** (2019) 074 [arXiv:1809.01179] [InSPIRE].

[133] A. Fradette, M. Pospelov, J. Pradler and A. Ritz, *Cosmological beam dump: constraints on dark scalars mixed with the Higgs boson*, *Phys. Rev.* **D 99** (2019) 075004 [arXiv:1812.07585] [InSPIRE].

[134] C. Boehm, P. Fayet and R. Schaeffer, *Constraining dark matter candidates from structure formation*, *Phys. Lett.* **B 518** (2001) 8 [astro-ph/0012504] [INSPIRE].

[135] A. Loeb and M. Zaldarriaga, *The small-scale power spectrum of cold dark matter*, *Phys. Rev.* **D 71** (2005) 103520 [astro-ph/0504112] [INSPIRE].

[136] T. Bringmann, H.T. Ihle, J. Kersten and P. Walia, *Suppressing structure formation at dwarf galaxy scales and below: late kinetic decoupling as a compelling alternative to warm dark matter*, *Phys. Rev.* **D 94** (2016) 103529 [arXiv:1603.04884] [INSPIRE].

[137] M. Vogelsberger, J. Zavala, F.-Y. Cyr-Racine, C. Pfrommer, T. Bringmann and K. Sigurdson, *ETHOS — an effective theory of structure formation: dark matter physics as a possible explanation of the small-scale CDM problems*, *Mon. Not. Roy. Astron. Soc.* **460** (2016) 1399 [arXiv:1512.05349] [INSPIRE].

[138] G. Krnjaic, *Probing light thermal dark-matter with a Higgs portal mediator*, *Phys. Rev.* **D 94** (2016) 073009 [arXiv:1512.04119] [INSPIRE].

[139] XENON collaboration, *First dark matter search results from the XENON1T experiment*, *Phys. Rev. Lett.* **119** (2017) 181301 [arXiv:1705.06655] [INSPIRE].

[140] G. Bélanger, F. Boudjema and A. Pukhov, *MicrOMEGAs: a code for the calculation of dark matter properties in generic models of particle interaction*, in *The Dark Secrets of the Terascale: proceedings, TASI* 2011, Boulder, CO, U.S.A. 6 June–11 July 2011, World Scientific, Singapore (2013), pg. 739 [arXiv:1402.0787] [INSPIRE].

[141] M. Kaplinghat, S. Tulin and H.-B. Yu, *Direct detection portals for self-interacting dark matter*, *Phys. Rev.* **D 89** (2014) 035009 [arXiv:1310.7945] [INSPIRE].

[142] THE GAMBIT DARK MATTER WORKGROUP collaboration, *DarkBit: a GAMBIT module for computing dark matter observables and likelihoods*, *Eur. Phys. J.* **C 77** (2017) 831 [arXiv:1705.07920] [INSPIRE].

[143] SUPERCDMS collaboration, *Low-mass dark matter search with CDMSlite*, *Phys. Rev.* **D 97** (2018) 022002 [arXiv:1707.01632] [INSPIRE].

[144] CRESST collaboration, *Limits on dark matter effective field theory parameters with CRESST-II*, *Eur. Phys. J.* **C 79** (2019) 43 [arXiv:1809.03753] [INSPIRE].

[145] SENSEI collaboration, *SENSEI: first direct-detection constraints on sub-GeV dark matter from a surface run*, *Phys. Rev. Lett.* **121** (2018) 061803 [arXiv:1804.00088] [INSPIRE].

[146] XENON collaboration, *Design and performance of the XENON10 dark matter experiment*, *Astropart. Phys.* **34** (2011) 679 [arXiv:1001.2834] [INSPIRE].

[147] XENON100 collaboration, *XENON100 dark matter results from a combination of* 477 *live days*, *Phys. Rev.* **D 94** (2016) 122001 [arXiv:1609.06154] [INSPIRE].

[148] SUPERCDMS collaboration, *First dark matter constraints from a SuperCDMS single-charge sensitive detector*, *Phys. Rev. Lett.* **121** (2018) 051301 [arXiv:1804.10697] [INSPIRE].

[149] DARKSIDE collaboration, *Low-mass dark matter search with the DarkSide-50 experiment*, *Phys. Rev. Lett.* **121** (2018) 081307 [arXiv:1802.06994] [INSPIRE].

[150] R. Essig, T. Volansky and T.-T. Yu, *New constraints and prospects for sub-GeV dark matter scattering off electrons in xenon*, *Phys. Rev.* **D 96** (2017) 043017 [arXiv:1703.00910] [INSPIRE].

[151] J. Billard, L. Strigari and E. Figueroa-Feliciano, *Implication of neutrino backgrounds on the reach of next generation dark matter direct detection experiments*, *Phys. Rev.* **D 89** (2014) 023524 [arXiv:1307.5458] [INSPIRE].

[152] A. Fradette and M. Pospelov, *BBN for the LHC: constraints on lifetimes of the Higgs portal scalars*, *Phys. Rev.* **D 96** (2017) 075033 [arXiv:1706.01920] [INSPIRE].

[153] M. D'Onofrio and K. Rummukainen, *Standard Model cross-over on the lattice*, *Phys. Rev.* **D 93** (2016) 025003 [arXiv:1508.07161] [INSPIRE].

[154] M. D'Onofrio, K. Rummukainen and A. Tranberg, *Sphaleron rate in the minimal Standard Model*, *Phys. Rev. Lett.* **113** (2014) 141602 [arXiv:1404.3565] [INSPIRE].

[155] J. Schieck et al., *Direct dark matter search with the CRESST II experiment*, PoS(ICHEP2016)217 (2016) [arXiv:1611.02113] [INSPIRE].

[156] SUPERCDMS collaboration, *New results from the search for low-mass weakly interacting massive particles with the CDMS low ionization threshold experiment*, *Phys. Rev. Lett.* **116** (2016) 071301 [arXiv:1509.02448] [INSPIRE].

[157] D.M. Asner et al., *ILC Higgs white paper*, in *Proceedings, 2013 Community Summer Study on the Future of U.S. Particle Physics: Snowmass on the Mississippi (CSS2013)*, Minneapolis, MN, U.S.A. 29 July–6 August 2013 [arXiv:1310.0763] [INSPIRE].

[158] SHiP collaboration, *A facility to Search for Hidden Particles (SHiP) at the CERN SPS*, arXiv:1504.04956 [INSPIRE].

[159] CMS collaboration, *Search for a light pseudoscalar Higgs boson in the dimuon decay channel in pp collisions at $\sqrt{s} = 7$ TeV*, *Phys. Rev. Lett.* **109** (2012) 121801 [arXiv:1206.6326] [INSPIRE].

[160] M. Lisanti and J.G. Wacker, *Discovering the Higgs with low mass muon pairs*, *Phys. Rev.* **D 79** (2009) 115006 [arXiv:0903.1377] [INSPIRE].

[161] B. Bhattacherjee, S. Matsumoto, S. Mukhopadhyay and M.M. Nojiri, *Phenomenology of light fermionic asymmetric dark matter*, *JHEP* **10** (2013) 032 [arXiv:1306.5878] [INSPIRE].

[162] M. Carena, T. Han, G.-Y. Huang and C.E.M. Wagner, *Higgs signal for $h \to aa$ at hadron colliders*, *JHEP* **04** (2008) 092 [arXiv:0712.2466] [INSPIRE].

[163] D. Curtin, R. Essig and Y.-M. Zhong, *Uncovering light scalars with exotic Higgs decays to $b\bar{b}\mu^+\mu^-$*, *JHEP* **06** (2015) 025 [arXiv:1412.4779] [INSPIRE].

[164] J. Alwall et al., *The automated computation of tree-level and next-to-leading order differential cross sections and their matching to parton shower simulations*, *JHEP* **07** (2014) 079 [arXiv:1405.0301] [INSPIRE].

[165] T. Sjöstrand, L. Lönnblad and S. Mrenna, *PYTHIA 6.2: physics and manual*, hep-ph/0108264 [INSPIRE].

[166] D. de Florian and J. Mazzitelli, *Higgs boson pair production at next-to-next-to-leading order in QCD*, *Phys. Rev. Lett.* **111** (2013) 201801 [arXiv:1309.6594] [INSPIRE].

[167] D. de Florian and J. Mazzitelli, *Higgs pair production at next-to-next-to-leading logarithmic accuracy at the LHC*, *JHEP* **09** (2015) 053 [arXiv:1505.07122] [INSPIRE].

[168] *LHC Higgs cross section HH sub-group webpage*, https://twiki.cern.ch/twiki/bin/view/LHCPhysics/LHCHXSWGHH.

[169] *HLT dimuon invariant mass distributions in* 2017 *and* 2018 *(CMS DP-*2018/055*) webpage*, https://twiki.cern.ch/twiki/bin/view/CMSPublic/HLTDiMuon2017and2018.

[170] CMS collaboration, *Data scouting & parking in CMS: its potential to search for LLP*, in fourth workshop of the LHC LLP community, Amsterdam, The Netherlands (2018).

[171] D. Curtin, R. Essig, S. Gori and J. Shelton, *Illuminating dark photons with high-energy colliders*, *JHEP* **02** (2015) 157 [arXiv:1412.0018] [ɪɴSPIRE].

[172] N. Bernal, X. Chu, C. Garcia-Cely, T. Hambye and B. Zaldivar, *Production regimes for self-interacting dark matter*, *JCAP* **03** (2016) 018 [arXiv:1510.08063] [ɪɴSPIRE].

[173] L.J. Hall, K. Jedamzik, J. March-Russell and S.M. West, *Freeze-in production of FIMP dark matter*, *JHEP* **03** (2010) 080 [arXiv:0911.1120] [ɪɴSPIRE].

[174] A. Biswas and A. Gupta, *Freeze-in production of sterile neutrino dark matter in* $U(1)_{B-L}$ *model*, *JCAP* **09** (2016) 044 [*Addendum ibid.* **05** (2017) A01] [arXiv:1607.01469] [ɪɴSPIRE].

[175] A. Biswas and A. Gupta, *Calculation of momentum distribution function of a non-thermal fermionic dark matter*, *JCAP* **03** (2017) 033 [*Addendum ibid.* **05** (2017) A02] [arXiv:1612.02793] [ɪɴSPIRE].

[176] N. Bernal, M. Heikinheimo, T. Tenkanen, K. Tuominen and V. Vaskonen, *The dawn of FIMP dark matter: a review of models and constraints*, *Int. J. Mod. Phys.* **A 32** (2017) 1730023 [arXiv:1706.07442].

[177] M. Blennow, E. Fernandez-Martinez and B. Zaldivar, *Freeze-in through portals*, *JCAP* **01** (2014) 003 [arXiv:1309.7348] [ɪɴSPIRE].